University of South Carolina

Scholar Commons

Theses and Dissertations

2017

Modeling Battery Performance Due To Volume Change In Porous Electrodes Due To Intercalation

Taylor R. Garrick
University of South Carolina

Follow this and additional works at: https://scholarcommons.sc.edu/etd

Part of the Chemical Engineering Commons

Recommended Citation

MODELING BATTERY PERFORMANCE DUE TO VOLUME CHANGE IN POROUS
ELECTRODES DUE TO INTERCALATION

by

Taylor R. Garrick

Bachelor of Science in Engineering
University of South Carolina, 2013

Submitted in Partial Fulfillment of the Requirements

For the Degree of Doctor of Philosophy in

Chemical Engineering

College of Engineering and Computing

University of South Carolina

2017

Accepted by:

John W. Weidner, Major Professor

Donna A. Chen, Committee Member

John R. Monnier, Committee Member

Sirivatch Shimpalee, Committee Member

Cheryl L. Addy, Vice Provost and Dean of the Graduate School

ACKNOWLEDGEMENTS

ABSTRACT

The demand for energy continues to increase as the economies of developing countries become more modern and show an increased need for a reliable energy infrastructure in order to meet the increased demand associated with a large and more mobile population. An increased demand puts a strain on all sectors, however it is specifically noticeable in the transportation sector where a significant portion of the fuel utilized for transportation comes from petroleum and other fossil fuels. Recently, using alternative forms of energy for transportation has become reality, and in turn, using electricity as a transportation fuel has gained significant momentum, specifically for use in battery-only rechargeable vehicles. Significant strides have been made to improve the range, cost, and fueling times of these battery-only vehicles through the improvement of the design and control of cells, and several automobile manufacturers are releasing battery powered vehicles with price points that target the general public. New materials have also been examined in order to increase the energy densities of these batteries in order to increase the range of battery powered vehicles, and decrease the volume displacement in the vehicle powertrain.

Some of the new battery electrode materials see significant expansion during cycling, which results in stress linked to capacity fade, battery failure, separator deformation, and electrolyte degradation. In order to accurately predict the behavior of complicated electrochemical devices undergoing a variety of different structural and electrochemical changes, sophisticated models that take into consideration transport

processes, electrochemical phenomena, mechanical stresses, and structural deformations must be developed in order to predict the associated effects on the operation of an electrochemical system. There are many models in the literature that can predict the electrochemical performance of devices with porous electrodes under a variety of operating and design conditions, however, in many of these models, when the porosity of the porous electrode is accounted for it is assumed to be a function of current density, since the volume changes seen during the intercalation reaction can be small. However, electrodes that have been developed in recent years show battery systems that have significant volume changes during intercalation. The battery model developed here incorporates aspects of a porous electrode model that accounts for the stresses that build up in porous electrodes due to volume change in the active material. The material balances here are coupled to stress-strain relationships that are derived from rock mechanics, in which the deformation of the porous rock occurs during thermal expansion similar to the deformation of the porous electrode that occurs during intercalation. This allows for a prediction of dimensional changes and porosity changes in a porous electrode and the associated effect on battery performance.

TABLE OF CONTENTS

LIST OF TABLES

LIST OF FIGURES

CHAPTER 1

INTRODUCTION

Due to the increase in energy demands in developing nations around the world, batteries that show an increased energy density have been the subject of much research in order to extend the operating time of consumer electronics and the range of new battery powered electric vehicles. The Li-ion battery has emerged during this time as the premier energy storage chemistry used in batteries for portable electronic devices as well as electric only battery vehicles due to the ability of many anode and cathode materials to incorporate large amounts of lithium into their structures. However, as the electric vehicle transportation market continues to grow, the need for batteries with higher energy density and longer cycle life is needed. This development of higher energy density materials has not been without setbacks[2] due to safety concerns[3-6], however, a renewed focus on safety has been implemented in newer batteries utilizing these high energy density materials.

Due to the recent commercial and government sector success of high energy density batteries, high performance electrode materials, separators, electrolytes, and new cell and stack designs are being actively developed. In commercial lithium-ion batteries, the most widely used positive electrode materials are typically metal oxides such as $LiCoO_2$[7-11] or $LiMnO_2$[12-15] and the most widely used negative electrode material is graphite[7, 11, 16-21]. Both positive and negative electrode materials react with lithium via intercalation.

During the intercalation reaction, lithium ions diffuse[20, 22-25] from the electrolyte into the active material and insert into the lattice structure of the active material, such as $LiCoO_2$. However, with some high expansion anode materials, such as silicon and tin, Li forms an alloy during the intercalation process, which involves the breaking of bonds and changes in the crystalline structure, and in turn results in significant expansion and structural deformation[26-31]. Due to the breaking of bonds during the intercalation alloying reaction in materials such as silicon and tin, as opposed to the non-alloying reactions seen in $LiCoO_2$ and graphite, the anode materials that see large expansion and high alloying have a much higher energy capacity. For example, the lithium-silicon alloy that contains the highest concentration of lithium is the $Li_{22}Si_5$[32-39] structure, which has a higher maximum lithium concentration than graphite[17, 19, 22, 40-42]. This high lithium concentration causes large volume changes[27, 43-46] which can result in fracturing of particles of active material causing capacity fade and resulting in rapid degradation of the electrode. Because of this, much work has been done to understand the changes in the Si crystalline structure during lithiation.

During the lithiation process, crystalline silicon is seen to have a reaction front that propagates through the silicon.[47, 48] This results in a large concentration difference between the front and back of the electrode, which causes significant strain that can result in localized and bulk stress in the system, resulting in fracture and electrode degradation. As the lithiation progress, several crystalline phases are seen to exist. These phases are $Li_{12}Si_7$[49], Li_7Si_3[50], $Li_{13}Si_4$[51], and $Li_{22}Si_5$.[52] These have been studied at high temperature by Wen et al.[52], but other groups have seen that low temperature lithiation and delithation of Si does not exhibit clear phases during cycling and rather shows a more

amorphous structure.[47, 48, 53, 54] This was further studied by Obrovac et al.[55] who discovered in the process that even though $Li_{22}Si_5$[51, 56] is the most lithium rich phase of Si[32-38], the phase reached at the final stages of lithiation is $Li_{15}Si_4$[55, 57] which is not an equilibrium phase, but is a stable crystalline phase where each Si is bonded to 12 adjacent Li atoms.[58] As seen here, significant crystalline changes occur in Si during lithiation and delithation.

As mentioned previously, these significant crystalline changes resulting large volume changes which cause significant degradation and capacity fade in silicon based electrodes.[7, 57, 59-63] Because of these diffusion induced stresses[64, 65] due to lithium concentration gradients, a significant amount of research has been done to develop models that can account for the strain and stress variation throughout a single particle, though the earlier models focused on materials that did not undergo stress and strain to the degree that is seen with Si. Christensen and Newman introduced a model that account for the stresses seen during volume expansion and contraction of a spherical particle that undergoes low volume change during intercalation.[26] Verbrugge has also developed models that account for time dependent diffusion induced stresses that arise.[66-73] However, in order to predict the behavior of electrochemical devices that undergo significant volume expansion, a move away from single particle models is necessary in order to take into consideration the bulk system and the associated effects of transportation processes, electrochemical phenomena, mechanical stresses, and structural deformations on the operation of a system with significant volume expansion during lithiation. Many other models in literature predict the electrochemical performance of devices containing porous electrodes under a variety of operating and design conditions.[9, 74-91]

In many of these models, the porosity of the porous electrode is often assumed constant, or when accounted for is assumed to be a function of current density only, since the volume changes seen during the intercalation reaction can be small. However, when using electrodes developed in recent years made of high expansion electrode materials, significant volume changes during intercalation do occur. For example, Jain et al.[75, 76] and Chandrasekaran and Fuller[81, 82] developed porous electrode models to account for changing porosity. Dimensional changes though were assumed to be negligible. A model to describe the volume change and account for porosity changes in porous electrodes was developed by Gomadam and Weidner[78], however, they assume an a priori split between these two. In order to predict the fraction of volume change that goes into porosity change, the prediction of the stresses in the porous electrode must be coupled to material balances.

Some of these models have been developed that couple volume expansion of the active material and stresses during intercalation and deintercalation.[26, 67, 70, 92] They reveal the importance that the change in volume plays in the generation of stresses and strains, and how this may be linked to experimentally observed failure in the active material. [29, 93, 94] However, these models incorporate many assumptions and do not consider how additional stress can build up in the system as the expanding electrode is being constrained by the battery casing.

More recently, work has been done to incorporate aspects of porous electrode theory and porous rock mechanics to account for the stresses that build up in porous electrodes with active material that undergoes significant volume change during intercalation.[1, 95] The material balances are coupled to stress-strain relationships derived from rock mechanics in which the deformation of the porous rock occurs during thermal

expansion. Other groups are using a force approach to stress and strain in porous electrodes and the associated effect on battery and battery pack performance.[95-104]

Through the use of bulk rock mechanics and bulk force measurements, battery models can be developed that account for significant stress and strain in electrodes using novel material that enables high energy density and long cycle life. These models can aid in the design of battery packs and help with extending the range of battery vehicles and the performance of consumer electronics.

CHAPTER 2

LITERATURE REVIEW

The battery considered in this work consists of two electrodes separated by a separator. The two electrodes contain the active material in the battery and in the case of a lithium-ion battery allow for the insertion and removal of lithium from the electrode matrix. During charge of a battery, the ions move out of the matrix in the positive electrode and diffuse to the separator, across the separator, into the negative electrode, and then insert into the matrix of the negative electrode. The literature covering the modeling of this phenomena in lithium ion batteries is quite extensive.

The first model to be developed containing two electrodes and a separator was presented by Fuller.[105] In this work, the galvanostatic charge and discharge of a dual lithium ion insertion cell was modeled. Transport phenomena were accounted for using concentrated solution theory with the assumption that transport could be modeled in a single dimension through the length of the positive electrode, separator, and negative electrode. The porous electrode was assumed to consist of inert material used as a binding, the electrolyte, and solid active insertion particles. The overall dimensions of the electrodes did not change. The modeling predictions were then compared to experimental results for a system with low single particle expansion observed during cycling.

More simplified models were developed by Newman and Doyle[106, 107] in order to present analytical solutions and considerations for design under different constraints. These models predicted discharge of rechargeable lithium ion batteries. The cell modeled

consisted of lithium manganese oxide, a polymer separator, and a lithium foil as reference. This model accounts for diffusion in the solid and electrolyte phases, as well as Butler-Volmer kinetics. This pseudo two dimensional (P2D) model is one of the most used models by battery researchers and allows for the user to solve for the electrolyte concentration, electrolyte potential, solid state potential, and solid state concentration within the porous electrodes, as well as allowing for the determination of the electrolyte concentration and electrolyte potential within the separator through the use of an extra dimension representing the particle radius. This model can easily be extended to a variety of different chemistries and has therefore led to the development of a number of different derivative models due to the low computational time needed to solve the representative partial differential equations governing the aforementioned phenomena. However, the dimensions of each electrode were assumed to be constant during discharge due to the small active material expansion seen in the electrode materials being modeled. Due to the simplification of the model as seen in Ref. [106], design considerations were accounted for that examined the utilization of capacity in the cell as well as the potential as a function of discharge as a tool for future battery design.

Arora and White[108] extended the model seen in Ref.[106] to examine lithium-ion polymer cells that have a higher active material loadings and competitive energy densities. Arora examined cells with different electrode thicknesses, different initial electrolyte concentrations, and modeled the associated transport processes in a plasticized polymer electrolyte system. Based on the work here, it was concluded that solution-phase diffusion limitations are the limiting factor during high-rate discharge. Because of this, a single diffusion coefficient was seen to be adequate for low discharge rates, while at high

7

rates, a variable diffusion coefficient and transport property data was needed to realize similarity between the mathematical model and experimental data. In this work, the dimensions of the electrodes were assumed to be constant during discharge due to the low expansion seen in the active material.

Doyle[109] continued this work and compared experimental data for a carbon negative electrode and a lithium manganese oxide positive electrode in a plastic lithium ion cell. The model showed good agreement to the experimental data on a variety of cell configurations. The model was then used to fit the diffusion coefficient of lithium in the carbon negative electrode as well as estimate other design parameters. The dimensions of the electrodes were assumed to be constant during operation. Simulations were again used to illustrate the effect of diffusion limitations on cell performance at high discharge rates and was extended to show the large effect of diffusion limitations on thicker electrodes and low electrolyte concentrations. The model was also used to confirm reversibility in the lithium ion insertion reaction. The effect of diffusion limitations on the diffusion in thicker electrodes is an important factor to consider when working with electrodes containing high expansion active materials because the thickness change could be significant during cycling.

Ning[110] extended the P2D model to derive a first principles model to simulate the cycling of rechargeable lithium ion batteries. This model accounts for the loss of lithium due to parasitic side reactions, as well as porous electrode theory, concentration solution theory, and takes into consideration kinetics and transport phenomena. The thickness of the electrodes and separator were assumed to be constant during cycling.

Ramadass[42] examined capacity fade in lithium ion cells through the development of a first principles based model that derives from the P2D model. The effect of the depth of discharge and the final voltage was considered to determine capacity fade. Parasitic reactions similar to Ref. [110] were considered as well as Butler-Volmer kinetics. Similar to previous works, a porous positive and porous negative electrode were considered with a separator. The dimensions of the electrode were assumed to be constant and porosity changes were not examined.

Separate work on a microscale was done by Zhang et al.[111] through the development of the single particle model which incorporated the effects of transport in a simple manner. This model accounted for diffusion and intercalation within a single spherical electrode particle, which was then expanded to consider the positive and negative electrode each as a single particle with the same surface area as the electrode under consideration.[90] In this model, diffusion and intercalation were accounted for within the particle, but the concentration and effect of potential was not considered in the solution phase between the particles. The porosity in the system was not examined, and the dimensions of the electrode under consideration were assumed to be constant. Due to the simplification of transport, the single particle model requires very little computation time, however, it is only valid for very low rates and thin porous electrodes.

Zhang and Sastry[112] simulated intercalation induced stress in lithium ion battery electrode particles that deviated from a spherical geometry. They modeled particle-level stress and strain during cycling in $LiMnO_4$ particles. The model approach included one dimensional simulations of spherical particles, three dimensional simulations of ellipsoidal particles, as well other particles of various shapes and sizes. Their results indicated that

large particle sizes and larger discharge current densities gave rise to larger intercalation-induced stresses, and that large aspect ratios in ellipsoid particle results in a reduction of intercalation induced stresses. A discussion of the advantages of intercalation induced stress on diffusion rates was also provided. They extended this model to simulate intercalation induced stress and heat generation in lithium ion battery cathode particles under potentiodynamic control.[74] The simulations seen in Ref. [74] indicated a non-uniform stress change with respect to intercalation. Initially, the intercalation induced-stress increased, and then decreased as the aspect ratio of the ellipsoidal particle increased. Here, aspects of thermal changes in porous materials were used to model the stress generation throughout the single particles, but the stresses and the effect on porosity throughout an electrode were not considered.

Park and Sastry[92] continued the simulation of stress in lithium ion battery cathode particles through the study of intercalation induced stresses and stresses due to phase transition in the electrode particle exemplified by the transition from the cubic to tetragonal phase in lithium manganese dioxide particles. In this model, stresses due to intercalation and phase transition in the single particle were predicted by relating the stress generation to particle geometry, lithium diffusion, and current density. The effect of concentration gradient in the particle on the stress generation was examined and determined to be a critical input on stress prediction during intercalation.

Golmon[113] developed a model for single particle stress that considered diffusion and surface kinetics to simulate the insertion of lithium into spherical silicon particles. The model predicted the change in concentration, dimensional change, and stress in the particles during insertion of lithium. Their work illustrates how the stress generated in the

10

silicon particle can exceed the stress needed to fracture based on the particle size and the relative rate of discharge compared to the rate of diffusion.

Cheng and Verbrugge[69] also modeled diffusion induced stress in spherical electrode particles and discussed the effects of material properties, transport phenomena, and structural mechanics on the stress in the particle. They also derived equations that predicted at what point cracking in the particle was likely to occur based on the maximum tensile strength of the electrode material. However, they did not consider dimensional changes in the bulk electrode.

As mentioned earlier, intercalation of lithium causes and expansion in the active material, such as graphite, manganese oxide, or silicon, while the extraction of lithium leads to contraction. Also, diffusion limitations significantly affect performance at higher discharge rates. Some groups have done work to model the diffusion of lithium into the electrode materials.[77, 114, 115] Gomadam[77] models the diffusion inside the electrode particles using a Fickian diffusion equation in spherical coordinates, shows that the solution phase diffusion limits cell performance, and determines that the value of the diffusion coefficient used in the simulation has a crucial effect on the ability of the model to predict the experimental data. Persson[114] used chronoamperometry with the Devanathan-Stachursky electrochemical method to quantify lithium diffusion in graphite anodes. They determined that lithium undergoes high diffusion parallel to the graphene plane and slow diffusion along grain boundaries. Kinetic Monte Carlo simulations were used to determine the diffusion coefficients of lithium as a function of concentration. Finally, Singh[115] developed a general continuum model to address intercalation dynamics in a single crystal battery electrode material representing $LiFePO_4$ which differs from the previous diffusion

11

limited model. Because lithium diffuses within the particle, the expansion of the active material does not happen uniformly, rather, the outside of the particle will expand faster than the inner portion of the particle.

As mentioned earlier, the stress that can be induced due to this expansion can cause fracturing and loss of the active material. Different models[26, 74] have been introduced to examine this volume change and stress induced via intercalation into single particles. For example, Christensen and Newman introduced a model that account for the stresses seen during volume expansion and contraction of a spherical particle that undergoes low volume change during intercalation.[26] In many of these models, the porosity of the porous electrode is often assumed constant or a function of current density only since the volume changes seen during the intercalation reaction can be small. However, when using electrodes developed in recent years made of high expansion electrode materials, significant volume changes during intercalation do occur.

In the past decade, models[75, 76, 81, 82] have been developed that account for changing porosity in a porous electrodes. The material balance typically used in one-dimensional mathematical models of porous electrodes is not valid when there is a volume change associated with the intercalation reaction. Jain[75] derived a variant of the material balance that accounts for a gain or loss in volume, as well as a change in the electrolyte volume. This equation was then applied to the prediction of capacity and electrolyte concentration and illustrates the need to account for volume changes in a cell. This model was then extended[76] to a spirally wound lithium chloride battery and used for parameter estimation and design studies and illustrated the need to account for volume loss in a cell during cycling. The material balance equation was combined with porous electrode theory

12

and concentration solution theory in order to estimate the diffusion coefficient and other parameters. The porosity however was assumed to be constant. Chandrasekaran[81, 82] developed models for lithium-silicon electrodes at room temperature that allow for volume change that is accounted for through porosity changes and not through dimensional changes. This enabled the modeling of concentration profiles within the electrode as well as the determination of diffusion within the electrode, and illustrated how diffusion and kinetics can limit the reaction in a cell at high discharge rates.

More recently, Gomadam and Weidner[78] developed a three dimensional mathematical model to account for volume changes in porous electrodes during operation. A material balance similar to Ref. [75] was used to account for volume change in the active material due to porosity changes, reaction product, and dimensional changes. A parameter, termed the swelling coefficient, was introduced in order to account for the relative magnitude of volume change going into porosity changes versus the magnitude of volume change going into dimensional changes, however, the split between volume change and porosity change would have to be measured experimentally, or predicted a priori. In order to predict the fraction of volume change that goes into porosity changes versus dimensional changes, the stress in the system must be coupled to material balances, which is the focus of this work.

CHAPTER 3

MODELING VOLUME CHANGE DUE TO INTERCALATION INTO POROUS ELECTRODES

In order to understand and accurately predict the behavior of electrochemical devices, it is necessary to develop sophisticated models that take into consideration transport processes, electrochemical phenomena, mechanical stresses, and structural deformations on the operation of an electrochemical system. There are many models in the literature that can predict the electrochemical performance of these devices (e.g., voltage versus time) under a variety of operating (e.g., current) and design (e.g., electrode thickness) conditions.

Porosity of the porous electrode is often assumed constant since the volume change during the intercalation reaction can be small.[116-119] Some battery systems though have significant volume change. For example, Alkire et al.[120] (copper dissolution), Dunning et al.[121] (zinc dissolution), Jain et al.[75, 76] (LiCl precipitation), and Chandreasekarar and Fuller[81, 82] (intercalation into silicon) developed porous electrode models to account for changing porosity. Dimensional changes though were assumed negligible. A model to describe the volume change in porous electrodes was developed by Gomadam and Weidner[78] to allow both porosity and dimensional change. However, they assumed an a priori split between these two. In order to predict the fraction of volume change in the active material that goes into porosity change, the prediction of the stresses in the porous electrode must be coupled to the material balances.

Models have been developed that couple volume expansion of the active material and stresses during intercalation and deintercalation.[122-126] They reveal the importance that the change in volume plays in the generation of stresses and strains, and how this may be linked to experimentally observed failure in the active material.[127-130] However, these models do not consider the porous nature of the electrode and how additional stress can build up in the system as the expanding electrode is being constrained by the battery casing.

The model developed here accounts for the stresses that build up in a porous electrode due to volume change in the active material. The material balances are coupled to stress-strain relationships derived from rock mechanics, in which the deformation of the porous rock occurs during thermal expansion[131]. The simulations shown here are for a single electrode where the reaction is uniform. However, the model is general and can be incorporated into porous-electrode theory to simulate the stresses that build up in a battery during cycling.

Model Development

During intercalation, the volume of the active material increases. The expansion can lead to a decrease in the porosity or an increase in the dimensions of the electrode. The extent to which porosity or dimensional change occurs depends on the stresses that build up in the porous electrode, and this is determined by the resistance of the electrode enclosure (i.e. casing) to dimensional change. Figure 3.1 illustrates the different cases that lead to a different mix of porosity changes. For the first case, the electrode volume is held constant by a rigid casing ($C_C = 0 \text{ GPa}^{-1}$) and all the volume change is forced to go into porosity changes. The rigid casing prevents dimensional changes. For the second case, the

casing offers no resistance and so all the volume change goes to changing the dimensions of the electrode. That is, the porosity remains constant because there are no forces enabling the particle to pack more tightly. Finally, for the third case, the casing offers some resistance to expansion and therefore the dimensions and porosity of the porous electrode vary during the intercalation and de-intercalation processes. A priori prediction of these volume changes and how they change during the intercalation process is critical to predicting the degradation of a battery.

As given previously[132], the relationship governing volume change in the electrode is obtained from an overall material balance on the solid active material and given below:

$$\frac{\partial}{\partial t}(1 - \varepsilon) + \boldsymbol{\nabla} \cdot [(1 - \varepsilon)\boldsymbol{u}] = -\frac{s\,\Delta\hat{V}}{nF}j \qquad [1]$$

The term on the right side of the equal sign is the volume change due to intercalating the reacting species into the active material (e.g., lithium into silicon). This volume change can cause either a change in porosity (first term on the left side of the equal sign) or dimensional changes (second term) expressed by the velocities of the control volume. Assuming the material expands equally in all directions, the velocity vectors can be replaced by the volumetric strain of the electrode, φ, resulting in a simplified version of Eq. [1]:

$$\frac{\partial}{\partial t}(1 - \varepsilon) + (1 - \varepsilon)\frac{\partial\varphi}{\partial t} = -\frac{s\,\Delta\hat{V}}{nF}j \qquad [2]$$

If the electrode is anisotropic, unequal expansion in different directions can be included and the treatment below can be applied to that more general material balance. The approach described here though will not change.

Taking into consideration rock mechanics[131], the compressibility of a porous electrode treated as a continuum of fractions of solid phase and pores can be defined as

$$C_E = -\frac{1}{V_m}\frac{dV_m}{d\sigma} \tag{3}$$

Where the subscript m on the volume denotes the portion of the electrode volume that changes due to mechanical forces within the porous matrix as opposed to volume change due to intercalation.

The volume of the porous electrode can be related to the strain by:

$$V_m = V_m^0(1 + \varphi) \tag{4}$$

where V_m^0 is the initial volume.

Solving Eq. [3] and Eq. [4] simultaneously, noting that the reaction current is constant such that $j = \frac{I}{V_{avg}}$, and adding strain due to intercalation (the last term on the RHS of Eqn 5.) allows the total electrode strain to be written in dimensionless form as,

$$\varphi = e^{(-\gamma\bar{\sigma})} - 1 + \left[\frac{\Delta\hat{V}}{\hat{V}_{avg}}\right]\tau \tag{5}$$

Where $\gamma = \frac{C_E}{C_c}$, is the ratio of the electrode compressibility to the casing compressibility, $\bar{\sigma}$ is dimensionless stress, and τ is the state of charge of the electrode (i.e., $\frac{tI}{Q_{max}}$).

It is assumed that there is no macroscopic separation or gap formation between and the electrode and the casing. This requires that the strain of the electrode has to be compatible with the expansion/contraction of the casing. An equivalent volumetric strain can be defined for the space enclosed by the casing. It is termed casing strain (φ_c), and it equals the total strain of the electrode. For small deformations, the casing strain can be assumed to be proportional to the stress and can be written as:

$$\varphi = \varphi_c = C_C\sigma \tag{6}$$

Note the casing strain defined here is not the actual mechanical strain of the skin of the casing. Here C_C is an equivalent compressibility of the casing. It represents the ratio of incremental volume strain of the casing to incremental internal pressure inside the casing. When φ_c is positive (expansion), the actual mechanical strain in the skin can have a negative component in the thickness direction and a positive membrane strain component. Eq. [5] and Eq. [6] allows the dimensionless stress to be solved for as a function of the state of charge, τ

$$\bar{\sigma} = \left[\frac{\Delta\hat{V}}{\hat{V}_{avg}}\right]\tau + \frac{1}{\gamma}\text{LambertW}\left(\gamma e^{-\left[\frac{\Delta\hat{V}}{\hat{V}_{avg}}\right]\tau\gamma+\gamma}\right) - 1 \qquad [7]$$

Where LambertW(x) is the Lambert W function, also known as the Omega function.[133]

Taking the derivative of Eq. [6] with respect to σ, multiplying Eq. [2] by $\frac{dt}{d\sigma}$, and combining the resulting equations yields the following expression in dimensionless form:

$$\frac{d(1-\varepsilon)}{d\bar{\sigma}} + (1-\varepsilon) = (1-\varepsilon^0)\frac{\left[1+\gamma e^{(-\gamma\bar{\sigma})}\right]}{[1+\bar{\sigma}]} \qquad [8]$$

Performing integration on Eq. [8] and assuming that $\varepsilon(0) = \varepsilon^0$ gives the analytical solution for porosity of the electrode as a function of stress.

$$\varepsilon(\bar{\sigma}) = (-\varepsilon^0\gamma e^{(\gamma-1)}\text{Ei}(\gamma-1-\bar{\sigma}(-\gamma+1)) + \gamma e^{(\gamma-1)}\text{Ei}(\gamma-1-\bar{\sigma}(-\gamma+1))$$

$$+e^{(\bar{\sigma})} + \varepsilon^{-1}\text{Ei}(-\bar{\sigma}-1) - \varepsilon^0\varepsilon^{-1}\text{Ei}(-\bar{\sigma}-1) + \varepsilon^0 + \varepsilon^0\gamma e^{(\gamma-1)}\text{Ei}(\gamma-1)$$

$$-\gamma e^{(\gamma-1)}\text{Ei}(\gamma-1) - 1 - \varepsilon^{-1}\text{Ei}(-1) + \varepsilon^0\varepsilon^{-1}\text{Ei}(-1))e^{(-\bar{\sigma})} \qquad [9]$$

Here Ei is the first order exponential integral function defined as[134]

$$\text{Ei}(x) = \int_x^{\infty} e^{-t}/t\, dt \quad \text{for } x > 0 \qquad [10]$$

Equations [5], [7], and [9] are solved simultaneously to give the stress (σ), porosity (ε), and dimensional change (φ) as a function of state of charge (τ). The solution is only a

18

function of γ and $\left[\frac{\Delta \hat{V}}{\hat{V}_{avg}}\right]$. It does not, for example, depend on discharge current since the reaction is assumed to be uniform. The stress, porosity and dimensional changes will, however, be a function of current once the equations are incorporated into porous electrode theory and/or diffusion resistance inside the active material is included.

Once the porosity and dimensional change are calculated, other properties of the porous electrode can be calculated. For example, the ionic resistance of the electrode can be obtained during the discharge by the following relationship derived previously.[132]

$$\frac{R}{R^0} = \frac{L \ /L^0}{(A \ /A^0 \ )(\varepsilon/\varepsilon^0)^{1.5}} \qquad [11]$$

where

$$\frac{L}{L^0} = \left(\frac{V}{V^0}\right)^{1/3} = (1 + \varphi)^{1/3} \qquad [12]$$

and

$$\frac{A}{A^0} = \left(\frac{V}{V^0}\right)^{2/3} = (1 + \varphi)^{2/3} \qquad [13]$$

In turn, the ionic resistance of the porous electrode can be used to estimate the effect of volume change on a discharge curve. For example, if the cell voltage takes the simple form of the Nernst equation minus the resistance of one porous electrode, the resulting equation is:

$$E = E^0 - 0.059\ln\left(\frac{\tau}{1-\tau}\right) - IR_i \qquad [14]$$

Finally, the results shown here can be compared to those from Gomadam et al.[132] by calculating a parameter they called the swelling coefficient, g, which is defined as the fraction of volume expansion that goes into the change in porosity. Therefore, $(1 - g)$ is the fraction that goes into the change in dimensions of the electrode. As stated earlier, their

model does not calculate this parameter a priori and so they set this value at the beginning of discharge and held it constant. Here, we can calculate the swelling coefficient throughout the intercalation by[132],

$$g = \frac{\frac{d\,lnV}{d\,ln(1-\varepsilon)}}{1+\frac{d\,lnV}{d\,ln(1-\varepsilon)}} \tag{15}$$

Using Eq. [4], Eq.[6], and Eq.[15], the swelling coefficient is given as

$$g = \frac{(1-\varepsilon)}{(1-\varepsilon^0)\left[1+\gamma e^{(-\gamma\bar{\sigma})}\right]-(1-\varepsilon)\bar{\sigma}} \tag{16}$$

Results and Discussion

As stated previously, Equations 5, 7, and 9 are solved simultaneously to give the stress (σ), porosity (ε), and dimensional change (φ) as a function of state of charge (τ). Since the reaction is assumed uniform throughout the porous electrode, no diffusional resistance occurs in the active material, and the stress is not a function of current. Rather, it only depends on the state of charge, the maximum strain of the active material, $\left[\frac{\Delta\hat{V}}{\hat{V}_{\text{avg}}}\right]$, and the ratio of the compressibilities of the porous electrode and casing ($\gamma = \frac{C_E}{C_C}$). For illustrative purposes, we simulate here the case where the volume expansion of the active material from the discharged to the charged state is 100% (i.e. $\left[\frac{\Delta\hat{V}}{\hat{V}_{\text{avg}}}\right] = 1$). This is similar to the expansion seen in silicon or tin anodes.[9]

Figure 3.2 shows the stress that builds up in the electrode as a function of state of charge and are plotted for the limiting cases for a rigid casing ($C_C = 0$), an infinitely compliant casing ($C_C = \infty$), as well as intermediate values that represent a metal ($C_C = 1\,\text{GPa}^{-1}$) and plastic casing ($C_C = 5\,\text{GPa}^{-1}$). When the casing is infinitely compliant (C$_C$

= ∞), there are no forces enabling the particles to pack more tightly and hence no stress builds up in the electrode. When the casing is rigid ($C_C = 0$), maximum stresses build up in the electrode. The stresses rise exponentially for the cases of finite casing compressibility as the electrode is charged, reflecting the exponential dependence of the stress versus strain shown in Eqn. [5]. For the other two casing compressibilities, the stresses build up exponentially, but do not reach a maximum due to moderate compliance seen in the casing.

The strain and porosity are plotted as a function of state of charge as seen in Fig. 3.3 and Fig. 3.4 respectively. Again, when the casing offers no resistance to expansion ($C_C = \infty$), all the volume change of the active material is translated into dimensional changes (i.e., strain) and the porosity remains constant. The linear increase is strain with respect to state of charge reflects the assumption that the volume of the active material is a linear combination of the completely intercalated ($\hat{V}_F$) and deintercalated ($\hat{V}^o$) molar volumes. When the casing is rigid ($C_C = 0$), expansion of the active material can only go into porosity changes because the dimensions of the cell are prevented from expanding. For intermediate values of casing compressibility, the initial change in strain and porosity are closer to the $C_C = 0$ case because the internal electrode stresses are not large enough to cause the casing to expand very much. Most of the volume change of the active material goes into porosity change. However, as the discharge progresses and internal stresses build up, the casing starts to expand and the changes in porosity level off.

The fraction of volume change that goes into dimensional changes compared to porosity changes can be seen more clearly in Fig. 3.5. Here the swelling coefficient defined by Gomodam and Weidner[10], and calculated in Equation 15, is plotted in Fig. 3.5 as a

function of state of charge. For rigid ($C_C = 0$) or infinitely compliant ($C_C = \infty$) casing, the volume expansion is either all porosity change ($g = 0$) or all dimensional change ($g = 1$), respectively. For low values of the casing compressibility (e.g., $C_C = 1$), the internal electrode stresses are not large enough to cause the casing to expand much early in the discharge. Hence most of the volume change of the active material goes into porosity change (i.e., $g=0.1$, or approximately 90% of the active material volume change goes into porosity change for $C_C = 1$). However, as the discharge progresses and internal stresses build up, the casing starts to expand and the changes in porosity level off. (i.e., at the end of discharge only 30% of the active material volume change goes into porosity change; $g = 0.7$). As C_C increases (i.e., casing is less rigid), a larger fraction of the volume change goes into dimensional changes throughout the discharge due to less resistance to expansion caused by a more compliant casing.

As indicated in Fig. 3.6, how g changes with state of charge is qualitatively similar for finite values of γ. The main difference is the value of g at the beginning of discharge (i.e. g^0). Therefore, the effect of γ (i.e. C_C at constant C_E) on the initial swelling coefficient g^0 is shown in Fig. 3.6 over a wide range of γ values. This figure shows that if the relative compressibility (γ) is small, then the electrode material will tend to direct the volume change towards dimensional change and if γ is large then the electrode material will tend to direct the volume change into changes in porosity. For cases discussed earlier, the relative compressibility is greater than 1 ($\gamma > 1$), which means that the casing is stiffer than the electrode. Due to this, the casing provides enough resistance to the volume change of the electrode and the intercalate volume is initially put towards filling the pores.

Knowing the dimensional and porosity changes of the electrode, properties such as ionic resistance can be calculated. Figure 3.7 is a plot of the dimensionless ionic resistance as calculated in Equation 11 for different values of C_C. When the casing is stiff ($C_C = 0$), all the pores are filled and the electrolyte is pushed out of the electrode, hence there is a rapid rise in ionic resistance as compared to when the casing is elastic. However, when the casing is infinitely compliant ($C_C = \infty$) the porosity remains constant during volume expansion, effectively decreasing the ionic resistance. For this case, the resistance actually decreases with purely dimensional change because the area over which the current flows increases faster than the electrode thickness increases. For the other two casing compressibilities, when the casing is more compliant, smaller changes in ionic resistance is seen since the porosity changes are smaller.

If the behavior of the electrode is assumed to be governed by ionic resistance, a simple discharge curve can be simulated using Equation 14. Figure 3.8 shows the cell voltage generated from Equation 14 for iRo = 0.1. For the cases where porosity changes are small (e.g., C_C is large relative to C_E), the voltage difference relative to the Nernst equation is fairly constant throughout the discharge since the ionic resistance is relatively constant (see Fig. 3.7). However, when the casing is relatively stiff (e.g., C_C is small relative to C_E), the porosity decreases during discharge, the ionic resistance rises rapidly, and hence the discharge voltage decreases rapidly.

Conclusions

A modeling approach has been established to predict the dimensional and porosity changes in a porous electrode cause by volume change in the active material during intercalation. The design parameter, g, is tracked throughout the processes in order to

23

account for the changes in dimensions and porosity. The development of this model was accomplished using a material balance over the electrode solid phase and principles from rock mechanics. The stress-strain relationships needed to predict porosity and volume changes have been established by examining the similarities between thermal rock expansion and electrode expansion due to intercalation. This approach can be integrated into a battery model based on porous electrode theory to extend the porous electrode models to accurately account for volume change effects.

Symbols

A	Cross-sectional area of porous electrode, cm^2
C	Compressibility, 1/Pa
E^0	Standard Cell Potential, V
E	Cell Voltage
$\mathcal{F}$	Faraday's constant, 96487 C/mol
g	Swelling coefficient
g_1	Splitting parameters for the dimension of the electrode in x_1 direction
g_2	Splitting parameters for the dimension of the electrode in x_2 direction
g_3	Splitting parameters for the dimension of the electrode in x_3 direction
I	Total applied current, A
j	Local volumetric electrochemical reaction rate, A/cm^3
$\bar{J}$	Dimensionless local volumetric electrochemical reaction rate
L	Electrode thickness, cm
n	Number of electron transfers in electrochemical reaction
$Q_{\max}$	Total charge of active material, $\left(\dfrac{V^0 nF}{s\widehat{V}^0}\right)$ C
R_{i,x_1}	Ionic resistance of porous electrode in x_1 direction, Ω

| s | Stoichiometric coefficient of the product in electrochemical reaction |

t Time, s

$\boldsymbol{u}$ Local velocity vector in the electrode, cm/s

V Total electrode volume, cm^3

$\hat{V}_{\text{avg}}$ Average molar electrode volume, cm^3/mol $\frac{\hat{V}_F + \hat{V}^0}{2}$

$\hat{V}_F$ Final molar electrode volume, cm^3/mol

$\hat{V}^0$ Initial molar electrode volume, cm^3/mol

$\hat{V}$ Molar volume of reaction product, cm^3/mol

Greek

ε Porosity

φ Volumetric strain

σ Hydrostatic stress, Pa

$\bar{\sigma}$ Dimensionless Hydrostatic stress, $C_C \sigma$

γ Relative compressibility

τ State of charge, $\frac{\tau I}{Q_{\text{max}}}$

Superscript

0 Initial

Subscript

C	Casing
E	Electrode
F	Final
m	Mechanical
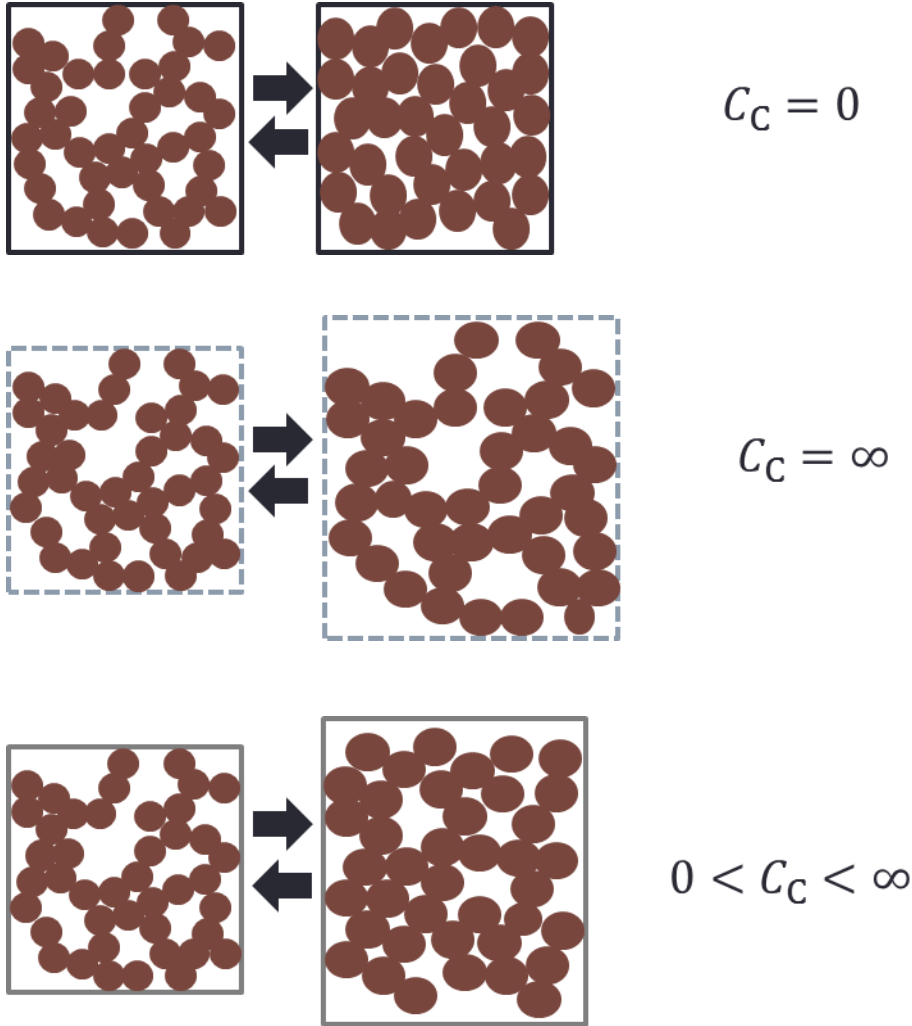
Figure 3.1: Depicts three cases with varying casing compressibility. Case #1 when the porous electrode is enclosed within an infinitely stiff casing, during intercalation there is no change in the volume of the electrode (g = 0). Case # 2 when the porous electrode is enclosed in an infinitely complaint casing, during intercalation there is only change in dimension of the electrode and the porosity of the electrode does not change (g = 1). Case # 3 when the porous electrode is enclosed in a finitely elastic casing, during intercalation both the dimensions and the porosity of the electrode change (0 < g < 1).
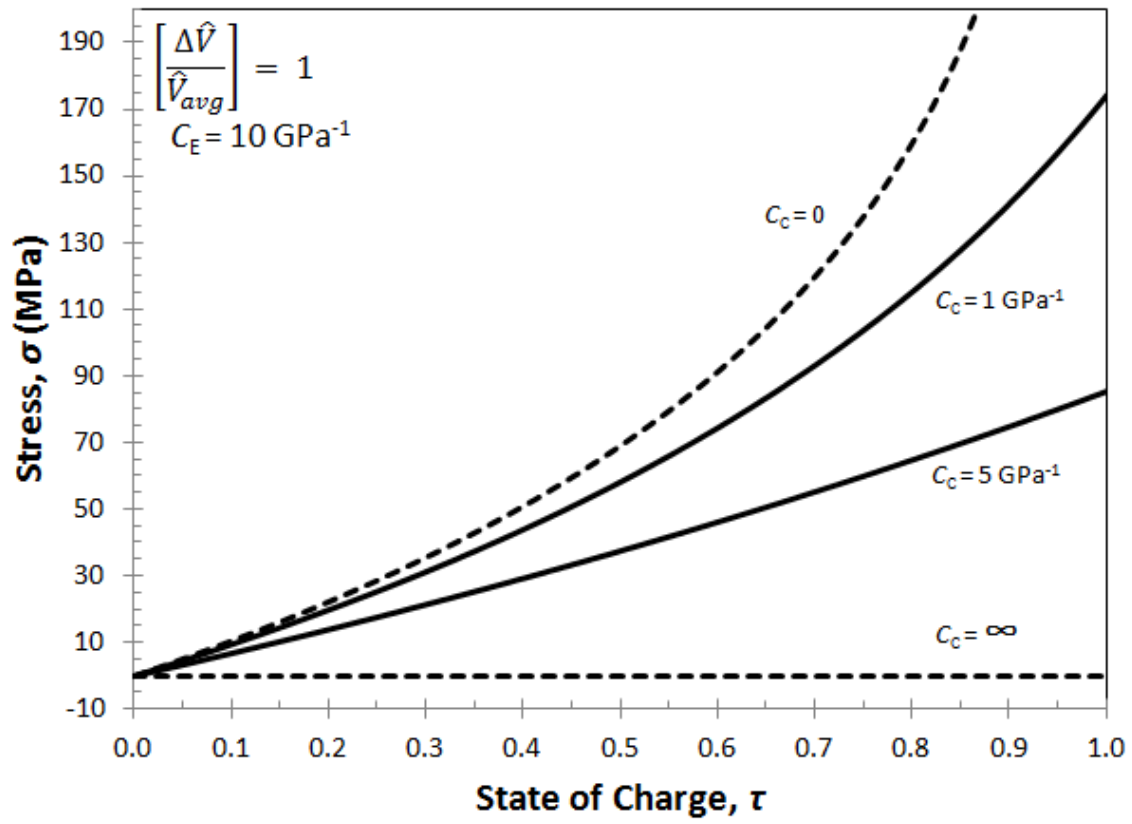
Figure 3.2: Stress building up in a porous electrode during intercalation for four values of the casing compressibility: rigid casing $(C_C = 0)$; infinitely compliant casing $(C_C = \infty)$; and two intermediate values.
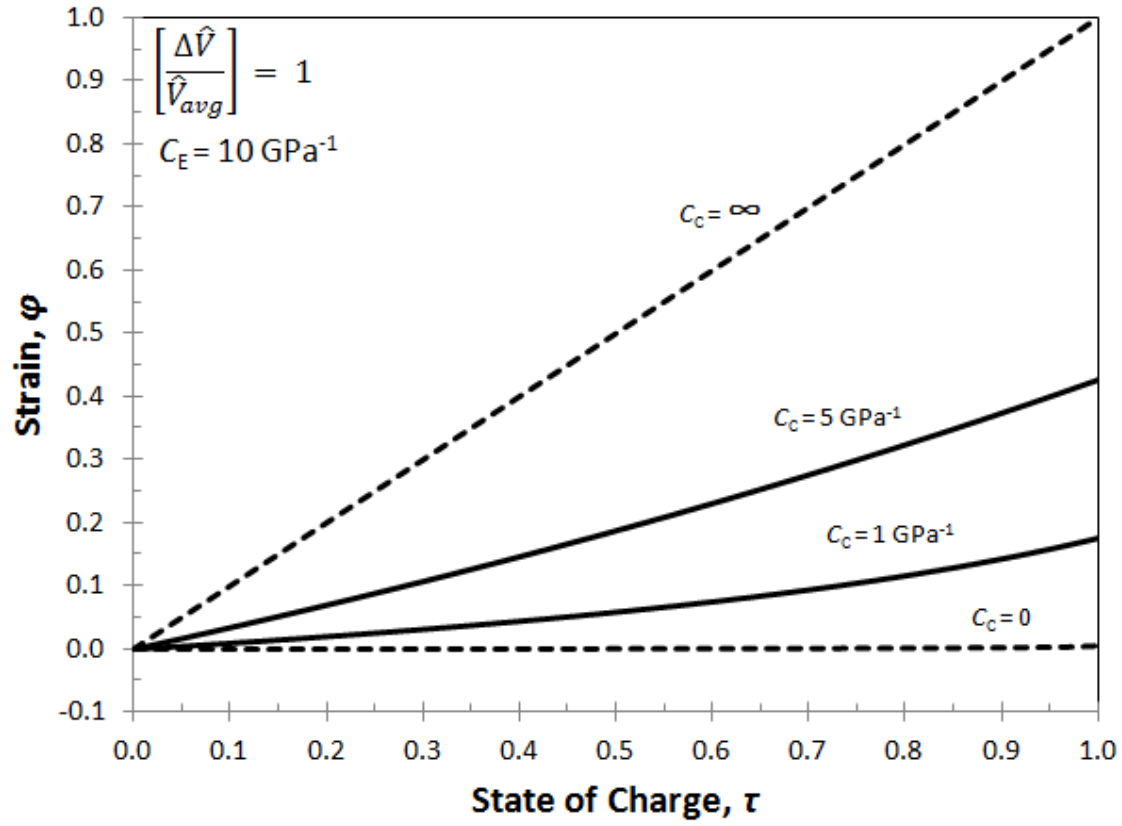
Figure 3.3: Strain in a porous electrode during intercalation for four values of the casing compressibility: rigid casing $(C_C = 0)$; infinitely compliant casing $(C_C = \infty)$; and two intermediate values.
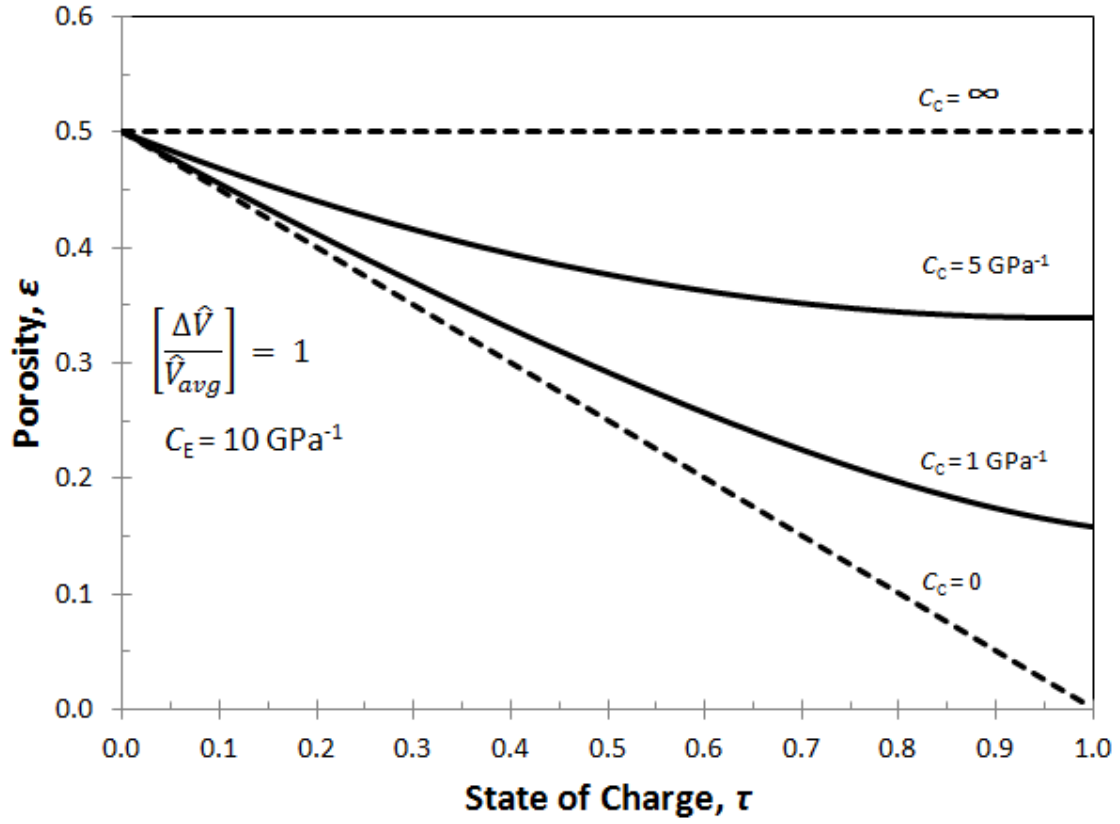
Figure 3.4: Porosity in a porous electrode during intercalation for four values of the casing compressibility: rigid casing $(C_C = 0)$; infinitely compliant casing $(C_C = \infty)$; and two intermediate values. Initial porosity, $\varepsilon^0 = 0.5$
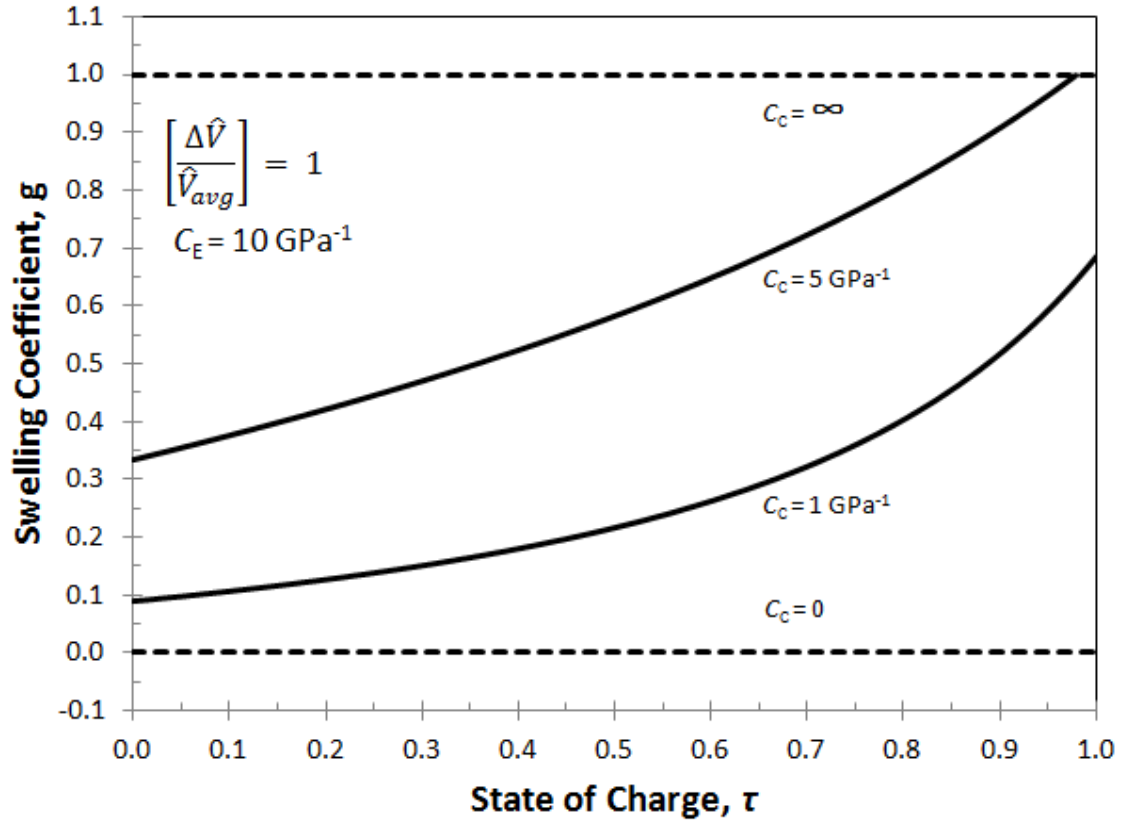
Figure 3.5: The swelling coefficient for a porous electrode during intercalation for four values of the casing compressibility: rigid casing $(C_C = 0)$; infinitely compliant casing $(C_C = \infty)$; and two intermediate values.
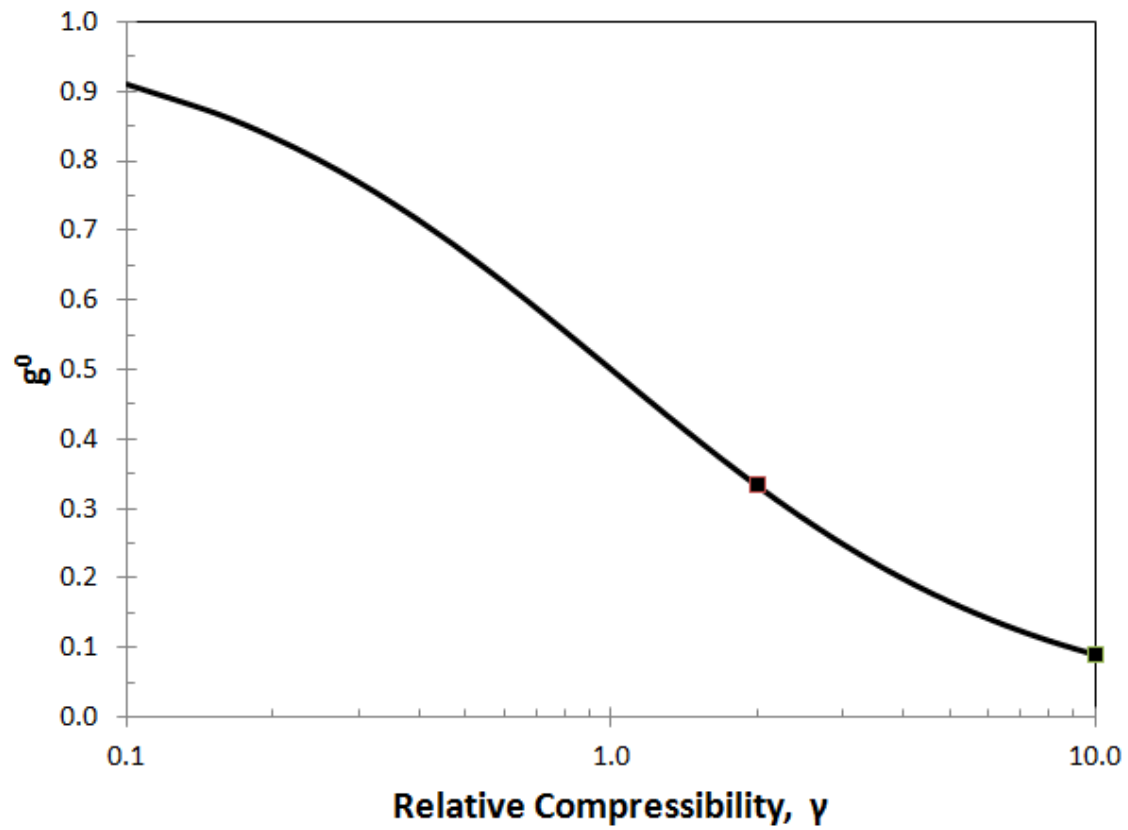
Figure 3.6: The initial swelling coefficient plotted as a function of the relative compressibility of a porous electrode, compared to that of the casing. ($\gamma = C_E/C_C$)
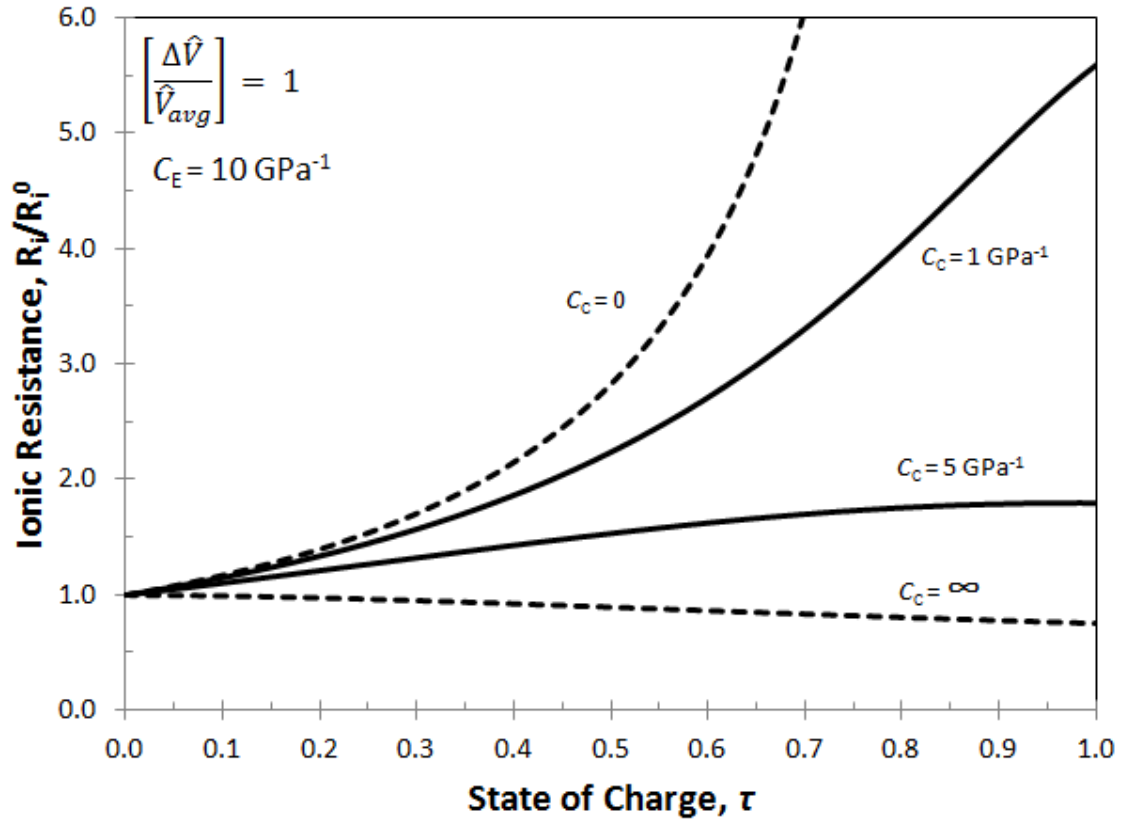
Figure 3.7: The ionic resistance in a porous electrode during intercalation for four values of the casing compressibility: rigid casing $(C_C = 0)$; infinitely compliant casing $(C_C = \infty)$; and two intermediate values.
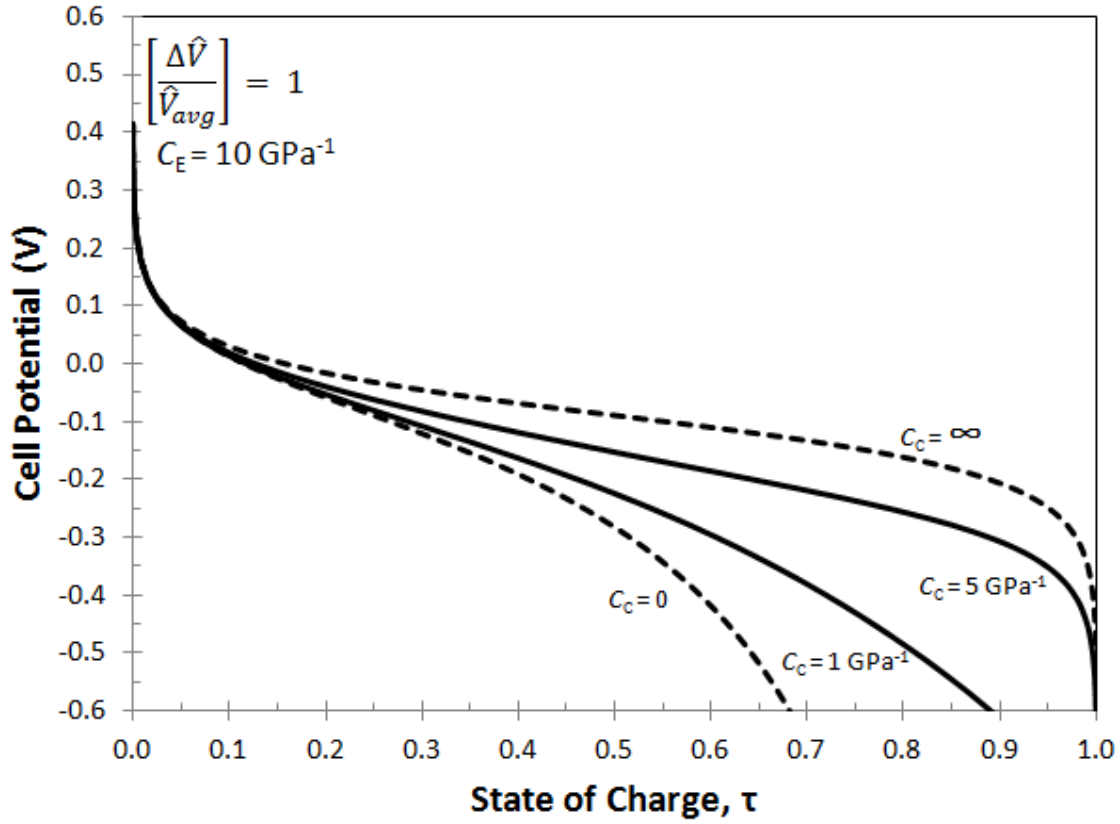
Figure 3.8: The discharge curve for an ideal electrode that takes the simple form of the Nernst equation minus the resistance of one porous electrode. $\frac{I}{V} = 0.1 \frac{A}{cm^2}$ Four values of the casing compressibility: rigid casing $(C_C = 0)$; infinitely compliant casing $(C_C = \infty)$; and two intermediate values.

CHAPTER 4

MODELING VOLUME CHANGE IN DUAL INSERTION ELECTRODES

Significant strides have been made to improve the range, cost, and fueling times of electric vehicles through the improvement of the design and control of cells, and several automobile manufacturers are releasing battery powered vehicles with price points that target the general public.[135-144] New chemistries, such as lithium ion, have also been examined in order to increase the energy densities of these batteries in order to increase the range of battery powered vehicles, and decrease the volume displacement of these batteries in the vehicle powertrain. However, because these new chemistries result in more energy in a smaller volume, safety problems may arise.[2] Therefore, it is critical to be able to predict the performance of new battery systems in order to improve safety and reliability, while also continuing to increase the energy density, which in turn decreases the weight and volume requirement of battery systems in alternative energy passenger vehicles.

Due to the recent commercial and government sector success of high energy density batteries, high performance electrode materials, separators, electrolytes, and new cell and stack designs are being actively developed to further improve cell capacity, charging and discharge rates, safety, cycle life, and shelf life. The most widely used anode material (graphite) in Lithium-ion batteries undergoes a volume change (10%) during lithiation and delithiation cycles.[43] However, high capacity anode materials, such as silicon and its alloys, undergo even higher volume changes ranging from 100% to 270%.[27, 43-45] Other battery chemistries, such as Li-Sn alloy intercalation cathodes, have seen volume

changes as high as 350% as observed by Yang et al.[145] The volume changes seen in these new battery electrode materials induce a significant amount of stress in the electrodes during battery operation.[1, 43, 78, 146] These volume changes and high stresses may result in the fracturing of active particles within the electrodes, and induces bulk stresses at the cell and stack level. A moderate amount of bulk stress in lithium-ion cells may be beneficial to cell operation, however, excessive stresses cause reduced cell performance, and cell damage. Recently, electrode stresses have been connected to the capacity fade in lithium-ion pouch cells.[147]

In order to accurately predict the behavior of electrochemical devices, it is necessary to develop sophisticated models that take into consideration transport processes, electrochemical phenomena, mechanical stresses, and structural deformations (i.e. strain) on the operation of an electrochemical system. There are many models in the literature that can predict the electrochemical performance of devices with porous electrodes (e.g. voltage vs time) under a variety of operating (e.g. current) and design (e.g. electrode thickness) conditions.[9, 26, 29, 67, 70, 74-80, 92-94, 148] In many of these models, the dimensions of the porous electrode are often assumed constant and any volume changes in the active material result in only porosity changes [75, 76]. Gomadam and Weidner[78] developed a model to allow both porosity and dimensional changes to occur. However, they assume an a priori split between these two. In order to predict the fraction of volume change that goes into porosity change, the prediction of the stresses in the porous electrode must be coupled to the material balances. Recently, models have been developed that couple volume expansion of the active material and stresses during intercalation and deintercalation of a single porous electrode.[26, 67, 70, 74, 92] They reveal the importance that a change in

volume plays in the generation of stresses and strains, and how this may be linked to experimentally observed failure in the active material.[29, 93, 94, 148]

The model developed here accounts for the stresses that build up in porous electrodes due to volume change in the active material through the application of porous rock mechanics to porous electrode theory. In previous models, a single electrode expanding against a casing with varying rigidity was examined[1, 78] in order to derive analytical expressions that governed the volume change in a single electrode. However, battery cells are composed of two electrodes which are required for operation, a positive electrode and a negative electrode. The presence of two electrodes affect the overall stress and strain observed in the system and show a deviation from the single electrode predictions seen earlier and are illustrated by the simulations shown here for the stress, strain, and porosity variations that can exist in a battery comprised of two porous electrodes and a compliant separator, enclosed in a semi-rigid casing. Uniform reaction rates throughout the porous electrodes are assumed in order to initially predict the interactions between the two electrodes without considering non-uniformities, which is valid for low discharge and charge rates. This addition of a second porous electrode that can compress and contract during the expansion of the other electrode more accurately accounts for the total dimensional changes of the battery. This enables us to examine the effects of relative thickness of the electrodes, relative active material expansion of the electrodes during cycling, and the tradeoff between stress and volume expansion in the system that can assist in realizing the benefits of these novel electrode materials, while accounting for the large volume changes that are associated with their use.

Model Development

Figure 4.1 illustrates the setup considered in this work. For illustrative purposes, the positive electrode is assumed to have an active material volume expansion during intercalation that is significantly larger than the active material volume expansion seen in the negative electrode during intercalation and deintercalation. This is similar to what would be seen in a single electrode study[53] if coupling a high expansion electrode material with a reference such as lithium, where the high expanding electrode is the positive electrode, and the reference is the negative electrode. In Figure 4.1 it is assumed that the separator is incompressible with fixed dimensions, and it is also assumed that there is no free space or gap between the electrodes, casing, and separator, but that a head space exists to allow for the inflow and outflow of electrolyte.

During discharge, charged particles intercalate from the negative electrode, resulting in a contraction of the negative electrode due to a decrease in the volume of the active material, into the positive electrode, resulting in an expansion of the positive electrode due to an increase in the volume of the active material. The opposite is true during charging.

As given previously[1, 78], the relationship governing the volume change in porous electrodes is obtained from an overall material balance on the solid active material and is seen below:

$$\frac{\partial(1-\varepsilon)}{\partial t} + \nabla \cdot [(1-\varepsilon)\boldsymbol{u}] = -\frac{s\Delta\widehat{V}}{nF}j \qquad [1]$$

The term on the right side of the equal sign is the volume change due to intercalating the reacting species into the active material. This volume change can cause either a change in porosity (the first term on the left side of the equal sign) or dimensional changes (second

term) expressed by the velocities of the control volume. Assuming one dimensional expansion, and uniform porosity across the length of each electrode, the velocity vectors can be replaced by the dimensional strain of the electrode, resulting in a simplified version of Equation 1:

$$\frac{\partial(1-\varepsilon)}{\partial t} + (1-\varepsilon)\frac{\partial\varphi}{\partial t} = -\frac{s\Delta\hat{V}}{nF}j \qquad [2]$$

Here, we assume low rates for charging and discharging, and therefore $j = I/V$. If the battery electrodes are anisotropic, unequal expansion in different directions can be included and applied to a more general material balance. Porous rock mechanic theory can be applied in these cases as well.

Taking into consideration rock mechanics[1], the compressibility of the two electrode system is treated as a continuum of fraction of the solid phase and pores and can be defined as:

$$C_E = -\frac{1}{V}\frac{dV}{d\sigma} \qquad [3]$$

The volume of the electrode under consideration as a function of strain can be derived from the definition of strain similar to what is seen in solid mechanics, assuming equal expansion in all directions, or uniform expansion in one direction:

$$V = V^0(1+\varphi) \qquad [4]$$

When solving Equations 3 and 4 simultaneously with the appropriate boundary conditions, the mechanical strain can be seen to be a function of electrode compressibility and stress and illustrates the change in dimensions due to stress on the electrodes:

$$\varphi_m = e^{-C_E\sigma} - 1 \qquad [5]$$

If no volume was added to the electrode due to intercalation, this equation would govern the strain of the electrode due to an applied pressure. However, similar to heating

in rock mechanics, the electrode expands with the addition of intercalate, and is therefore also a function of the intercalation of ions into the matrix:

$$\varphi_i = \left[\frac{\Delta\widehat{V}}{\widehat{V}^0}\right]\tau \qquad [6]$$

The expansion as a function of state of charge is known for certain substances, and in this instance, $\left[\frac{\Delta\widehat{V}}{\widehat{V}^0}\right]$ could be a function of the state of intercalation, and Equation 6 would still be valid. This model is assumed to be galvanostatic, and τ is defined accordingly:

$$\tau = \frac{tI}{Q_{max}} \qquad [7]$$

With the system defined here, as seen in Figure 4.1, the porous positive electrode is assumed to expand during discharge and contract during charge. Therefore, τ refers both to the state of intercalation of charged species into the positive electrode, as well as the state of discharge of the system. $1 - \tau$ therefore is equal to the state of charge of the battery. The strain of the positive electrode is then defined by combining Equations 5 and 6 as follows:

$$\varphi_+ = \varphi_m + \varphi_i = e^{-C_{E+}\sigma} - 1 + \left[\frac{\Delta\widehat{V}}{\widehat{V}^0}\right]_+\tau \qquad [8]$$

The strain of the negative electrode is then defined as:

$$\varphi_- = \varphi_m + \varphi_i = e^{-C_{E-}\sigma} - 1 + \left[\frac{\Delta\widehat{V}}{\widehat{V}^0}\right]_-(1-\tau) \qquad [9]$$

The strain of each electrode can then be used to determine the overall strain inside the battery. Here, we assume that the strain develops in one direction, and the following equation is reduced to consider initial thicknesses, however, initial volumes could be used instead of initial thicknesses if strain in three dimensions is considered.

$$\varphi_{battery} = \frac{(\varphi_++1)L_+^0+(\varphi_{sep}+1)L_{sep}^0+(\varphi_-+1)L_-^0}{L_+^0+L_{sep}^0+L_-^0} - 1 \qquad [10]$$

An equivalent volumetric strain can be defined for the space enclosed by the casing. It is termed casing strain and is equivalent to the total strain of the combined electrodes. For small deformations in the absence of free space, the casing strain can be assumed to be proportional to the electrode strain, and in turn the bulk stress. When free space exists inside the battery casing, the casing strain and total electrode strain are not equal, rather, the casing strain is equal to zero while the total electrode strain varies, up until the point at which the expansion and contraction of either or both electrodes fills the free space. The casing strain is therefore written as follows and is equal to the strain of the electrode system when no free space is present:

$$\varphi_{battery} = \varphi_c = C_C \sigma \qquad\qquad [11]$$

The casing strain as defined here is not the mechanical strain of the casing, rather C_C is an equivalent compressibility of the casing and represents the ratio of incremental volume strain of the casing to incremental internal pressure inside the casing. When φ_c is positive during expansion, the actual mechanical strain in the casing or separator can have a negative component in the thickness direction and a positive membrane strain component.

Combining Equations 10 and 11 allows the dimensionless hydrostatic stress of the dual electrode system to be solved for as a function of the state of intercalation of the expanding electrode in the battery, similar to what is seen for a single electrode. Once the hydrostatic stress is known, the strain of each individual electrode can be predicted by substituting in the hydrostatic stress. Combining the material balance seen in Equation 2 with boundary conditions as seen in previous work[1] a solution for porosity of each electrode as a function of state of intercalation and the hydrostatic stress in the system. The porosity then only depends on the known properties of each porous electrode (i.e. initial

molar volume, final molar volume, electrode compressibility, and initial porosity) as well as the compressibility of the battery casing. The representative figures seen here do not depend on the current distribution because the reaction is assumed to be uniform. Later works will incorporate non-uniform reaction distributions and non-uniform concentration changes, and the stress, porosity, and dimensional changes will be a function of current once the volume change equations are incorporated into porous electrode models or diffusion resistance inside the active material is included.

When working within the assumptions made in this work, Equation 11 can be used as a design equation in order to quickly determine or predict mechanical properties needed in the hardware and electrodes in order to meet design considerations, such as stress and casing strain limits, or the effect of materials that have different single particle expansion. For discussion purposes, an expanded form of Equation 11 is shown here:

$$\varphi_c = C_C \sigma = \frac{(\varphi_+ + 1)L_+^0 + (\varphi_{sep} + 1)L_{sep}^0 + (\varphi_- + 1)L_-^0}{L_+^0 + L_{sep}^0 + L_-^0} - 1 \qquad [12]$$

For simplicity, the positive electrode was assumed to be the expanding electrode, however, the results would be identical if the negative electrode was assumed to be the expanding electrode, and charging was being examined instead of discharge.

In order to illustrate the applicability of Equation 12 during the design phase, a range of parameters were chosen for this work and are summarized in Table. In Figures 4.2-4.4, the compressibility ratio was chosen in order to examine a very rigid and very compliant constraint on the expanding electrode as well as to show a comparison to previous work.[1] For the remaining figures, the compressibility ratio is implied based on the strain considered, but is infinite in certain settings in order to illustrate a very rigid or constrained system, and is varied in others to illustrate the effect. For all figures, the

43

expanding electrode single particle expansion, $\left[\frac{\Delta \hat{V}}{\hat{V}^0}\right]$, was chosen to be 1 because it is on the order of high expansion electrode materials such as silicon or tin, and is useful for comparison to previous work.[1] If $\left[\frac{\Delta \hat{V}}{\hat{V}^0}\right]$ was set higher, then the stress and strain would have higher magnitudes than currently shown. The contracting single electrode particle expansion was chosen in Figures 4.2-4.4 to illustrate the addition of a secondary electrode and focus on the compression of the secondary electrode, rather than the contraction due to the removal of charged species. Also, many materials that are available to be coupled to high expanding electrode materials undergo qualitatively smaller volume changes during lithiation and delithiation. The initial expanding electrode thickness, L_+^0, was chosen based on previous work[149], and is irrelevant for the mechanical studies seen here, but significant when considering the effect of conductivity and diffusion when examining higher rates in future work. The initial contracting electrode thickness was chosen based on previous work[149] for Figures 4.2-4.4,4.8, and was varied relative to the initial expanding electrode thickness in order to show the effect of different length ratios in Figures 4.5-4.7. The separator thickness was taken from previous work.[149] The initial porosity was taken from previous work[1] to aid in comparison, and would be varied in a real system in order to more closely match the capacities of each electrode, but does not have an effect on the stress and strain generated in the system based on the rock mechanics treatment, and was therefore not varied in this work. Lastly, the state of intercalation was chosen for comparison to previous work[1] for Figures 4.2-4.4, and set at 1 for the remaining figures due to this state illustrating the highest stress and strain in the system.

Results and Discussion

Figures 4.2-4.4 show the stress, strain and porosity changes in the expanding electrode as a function of state of charge (solid lines). For comparison, these three figures show the results from our previous work[1] (dashed lines), where there is only one electrode (i.e., no corresponding contracting second electrode).

Figure 4.2 shows the increase in stress as the charged species are inserted into the matrix of the expanding electrode. This is due to the increase in volume in the active material expanding against the contracting electrode and/or the cell casing. When comparing the stress increase between a single electrode system and a dual electrode system, it can be seen for identical $\frac{C_{E+}}{C_C}$ values, the presence of a secondary electrode results in the relieving of some of the stress observed in the single electrode system. This is due to the compression of the secondary electrode (negative electrode in Figure 4.1) allowing for higher volume change in the expanding electrode. Decreasing the $\frac{C_{E+}}{C_C}$ value is also seen to have a similar effect on the overall stress generation, with lower $\frac{C_{E+}}{C_C}$ values representing more compliant casings and therefore resulting in lower stress generation when compared to higher $\frac{C_{E+}}{C_C}$ values representing an increase in casing rigidity (decrease in casing compressibility). This combination of secondary electrode selection and casing rigidity selection can have a significant effect on the stress in the system. As seen here, increasing the casing compressibility and adding a secondary electrode serves to decrease the final hydrostatic stress in the system from ~174 MPa to ~44 MPa.

Figure 4.3 shows the strain development as a function of state of intercalation in a two electrode system compared to the strain development predicted in a single electrode

system in earlier works.[1] As seen in the dual electrode system represented by the solid lines, as particles are inserted into the active material of the expanding electrode, volume change occurs resulting in an increase in the strain of the expanding electrode. This is coupled to the contraction and compression of a secondary electrode. When compared to a single electrode system with identical $\frac{C_{E+}}{C_C}$ value, the strain the expanding electrode can be seen to increase more rapidly than its single electrode counterpart. This is due to the presence and compression of a secondary electrode as seen in Figure 4.1 which serves to allow for an increase in the volume expansion of the expanding electrode. When decreasing the casing rigidity (decrease in $\frac{C_{E+}}{C_C}$), the strain in the expanding electrode increases more rapidly due to the shift in volume changes from porosity changes towards dimensional changes associated with the decrease in stress as seen in the earlier figure. These strain changes are also significant considerations when designing a battery pack. With the advent of newer electrode materials that undergo significant volume change, vehicle manufacturers want to take advantage of the increased energy density while still minimizing the volume used in the vehicle for battery pack storage. Therefore, the strain of each electrode, and the corresponding strain of the entire system must be considered and modeled in order to aid in the design of battery packs. If the strain in the cell is too large, this could cause degradation of the battery pack components over time, resulting in loss of electrical contact to the cell, or cracking of the battery pack casing. Significant strain could also result in the rupture of the cell packaging and leakage of the electrolyte and other cell components.

Figure 4.4 illustrates the porosity changes in the expanding electrode in a dual electrode system as a function of intercalation compared to the porosity changes in a single

electrode system modeled in earlier work.[1] Seen here, as the state of intercalation of the system increases, the porosity is seen to decrease in the expanding electrode. This is due to an increase in the stress in the system as seen earlier in Figure 4.2 resulting in forcing volume changes to go into porosity changes. When comparing a dual electrode system and a single electrode system with identical $\frac{C_{E+}}{C_C}$, it can be seen that the porosity does not decrease as rapidly in the dual electrode system. This is due to lower stresses in the dual electrode system tied with higher strain in the expanding electrode resulting in volume changes going towards dimensional changes and relieving the volume changes going towards porosity changes. When increasing the $\frac{C_{E+}}{C_C}$, the casing is more rigid, resulting in more volume changes going towards porosity changes, and in turn a lower porosity at the end of intercalation. The porosity changes are also an important parameter to consider when designing a cell and battery pack, because if the overall porosity is too low, or if porosity changes during use are too large, high rate charge or discharge can be inhibited, resulting in loss of available range or a decrease in performance.

As discussed, many different parameters must be considered when designing a cell and a battery pack. Stresses and strains in an individual cell can cause degradation within the cell, but can also result in material degradation in the battery housing and the battery pack. During design phases for production vehicles and battery packs, modeling predictions are heavily used in order to meet vehicle design deadlines and minimize the amount of testing necessary to obtain model parameters for vehicle simulation. To this end, Equation 12 offers the ability to determine material characteristics based on rock mechanics principles in order to meet battery cell and pack design constraints.

Figure 4.5 shows the effect of the electrode compressibility ratio ($\frac{C_{E+}}{C_{E-}}$) on the overall dimensionless stress observed in the system for an expanding electrode undergoing significant volume change during insertion of lithium constrained by a rigid casing or a set maximum strain as would be typical in a battery pack. Here, the compressibility of the expanding electrode was set as the reference for the dimensionless stress, i.e. $\bar{\sigma} = \sigma \cdot C_{E+}$. The effect of initial length ratios between the expanding and contracting electrodes is also considered. This length ratio may need to be varied in order to match the capacities of the electrode materials under consideration in order to realize the full capacity of both electrodes, or may be varied in order to cycle over a small state of charge in one electrode in order to minimize lithium plating or other physics resulting in capacity loss. Here, as $\frac{C_{E+}}{C_{E-}}$ is increased (the rigidity of the contracting electrode is increased compared to the rigidity of the expanding electrode), the stress in the system at the final state of intercalation is predicted to increase. This stress increase is due to the restriction of volume expansion in the cell, resulting in more volume change being forced into porosity changes compared to dimensional changes. As the length ratio is increased, as would be typical if changing the volume of either electrode in order to match capacities, or trying to cycle over a small state of charge for performance reasons, the stress in the system is also observed to increase at the final state of intercalation across all electrode compressibility ratios. Here, if one desires to maximize the dimensional change of the expanding electrode during intercalation in order to utilize the high capacity offered by that material, a cell with a very compressible secondary electrode would be desired in order to relieve stresses in the system, regardless of the ratio of initial electrode lengths. Looking at Figure 4.1, this would mean that the positive electrode is expanding into a compressible negative electrode with a shift of the

separator to the right as the negative electrode decreases in dimension. However, if the secondary electrode needed to be very rigid and the overall volume available for the individual cell was restricted due to battery pack design constraints, one could easily predict the increase in stress and determine if it fell within the allowed stress in the battery pack.

These stress variations can also have a significant effect on the overall design of an electric vehicle from a materials standpoint. For example, when designing battery packs, one must keep moderate stress on the batteries in the pack to keep them from working loose during use, causing degradation of the electrical contacts and failure of the battery pack. Significant generated stresses by each cell can result in cracking of the battery pack material, or irreversible compression of the spacers and heat transfer devices, resulting in pack failure or runaway thermal conditions.

Figure 4.6 illustrates the dimensionless stress as a function of the final casing strain and initial electrode length ratio. As the allowed casing strain is increased (an increase in the dimensions of the cell seen in Figure 4.1), corresponding to the allowed casing expansion in the battery pack, the stress in the system decreases. This is due to a shift in volume changes towards dimensional changes in the expanding electrode (positive electrode in Figure 4.1) away from volume changes going towards porosity changes. When considering a case with $\frac{L_+}{L_-} = 1$, the maximum stress that could be reached with a very rigid enclosure or very limited pack space is 1.1. For the same system, ensuring that there was enough volume to allow the cells in the battery pack to expand by 28% would minimize the stresses in the cell and on the cell's surroundings. As seen here, significant weighting in initial length towards the high expanding electrode ($\frac{C_{E+}}{C_{E-}} = 4$) would still only realize a

maximum overall strain of 0.7 (70%) expansion from the initial state. Modeling this stress and strain tradeoff is integral in the initial design stages of battery modules and battery packs in order to minimize degradation in the cell and degradation of the battery pack materials.

Figure 4.7 shows the dimensionless stress as a function of the single particle expansion ratio between the contracting electrode and the expanding electrode. As the ratio increases, a decrease in the predicted stress is observed. This is due to a more rapid contraction of the secondary electrode (negative electrode in Figure 4.1) compared to the dimensional change of the expanding electrode (positive electrode in Figure 4.1), resulting in a minimization of the generated stresses. An increase in the initial electrode length ratio also sees an increase in the stress at the final state of intercalation. Seen here are two representative cases illustrating the practicality of this prediction. The circle represents the case of lithium intercalation from an electrode similar to a $LiCoO_2$ electrode into a graphite/silicon composite electrode. It is assumed that the composite electrode is undergoing an assumed expansion of 100% observed in the composite electrode active material and an assumed active material expansion of 3% in the positive electrode. Also, the expanding electrode is 2/3 of the initial length of the contracting electrode. In Figure 4.6 it can be seen that these conditions predict a dimensionless stress of 0.48. When considering the case of intercalation from a $LiCoO_2$ electrode into a graphite electrode, represented by a square in Figure 4.6, it can be seen that for the single particle expansion ratio of 0.3 for this system, the dimensionless stress is predicted to be 0.83. A figure such as this could be generated for any chemistry and could be used to determine the mix of chemistry in a particular electrode in order to meet stress targets in the system.

50

Taking the previous 3 figures and Equation 12 into consideration allows for the user to determine the stress in the cell as a function of a variety of material properties such as casing and electrode compressibilities, initial internal component thicknesses, and the total allowed volume expansion in the system. Once the dimensionless stress is known, the porosity can easily be determined for either electrode in the system. Figure 4.8 illustrates the porosity of the expanding electrode at the final state of intercalation as a function of the dimensionless stress in the system and the total expansion of the expanding electrode at the final state. This is a representative figure generated through the use of Equation 2 and can be generated for any cell design desired. Here, the porosity of the expanding electrode is seen to decrease as a function of dimensionless stress generated in the system at the final state of intercalation. The porosity of the system decreases rapidly as the final stress is increased, but levels off due to the need for higher amounts of applied stress to affect the same amount of porosity change in the system. The solid line represents a system similar to the single electrode expansion in Ref. [1] where a rigid casing completely restricts volume changes to porosity changes and does not allow for any dimensional changes in the electrode. Depending on the secondary electrode added, specifically with respect to the compressibility and contraction during delithiation, the strain change in the expanding electrode increases. As the strain in the expanding electrode increases at the final state of lithiation, an increase in the porosity is predicted due to more volume changes going towards dimensional changes and less going towards porosity changes. The porosity predicted here can be integrated into a variety of industrial design software packages to estimate the electrochemical performance of a cell or battery pack during use.

51

Conclusion

A modeling approach has been extended to a two electrode system to predict the dimensional and porosity changes caused by volume change in the active material during intercalation and make a comparison to a single electrode system. Stress-strain relationships that were obtained from examining the similarities between thermal rock expansion and electrode expansion due to intercalation were used to link the stress to material balances. The model equations were then used to generate summary figures illustrating considerations that must be examined when working with electrode materials that undergo significant expansion. This approach can be integrated into a more complex battery model based on porous electrode theory in order to accurately account for volume change effects. The work seen here can aid in the design and realization of batteries for use in alternative energy vehicles.

Symbols

C_C Casing compressibility, 1/GPa

C_E Electrode compressibility, 1/GPa

F Faraday's constant, 96485 C/mol

I Applied current

j Current density, A/cm^3

L Length or thickness, cm

n Electrons transferred in the reaction

Q_{max} Capacity, mAh

s Stoichiometric coefficient

t Time, s

$\boldsymbol{u}$ Electrode velocity, cm/s

$\hat{V}$ Molar volume, cm^3/mol

V Electrode volume, cm^3

V^0 Initial electrode volume, cm^3

Greek

ε Porosity

φ Volumetric strain

σ Stress, GPa

$\bar{\sigma}$ Dimensionless Stress, $(\sigma \cdot C_{E+})$

τ State of charge or intercalation

Subscripts and Superscripts

0   Initial

+   Expanding electrode

-       Contracting electrode

c   Casing

sep   Separator

Table 4.1 List of parameters used with Equation 4.8, 4.9, and 4.10 for Figures 4.2-4.8

Figure	Figure 4.2	Figure 4.3	Figure 4.4	Figure 4.5	Figure 4.6	Figure 4.7	Figure 4.8
Compressibility ratio	2, 10			Infinite (Strain = 0)	Function of Strain	Infinite (Strain=0)	Function of Strain
Expanding Electrode Single Particle Expansion	100%						
Contracting Electrode Single Particle Expansion	0.05			0		Varies	0
Initial Expanding Electrode Thickness	6.8×10^{-5} m						
Initial Contracting Electrode Thickness	6.8×10^{-5} m			Varies	Varies	Varies	6.8×10^{-5} m
Separator Thickness	5×10^{-5} m						
Initial Porosity	0.5						
State of Intercalation	0-1			1			
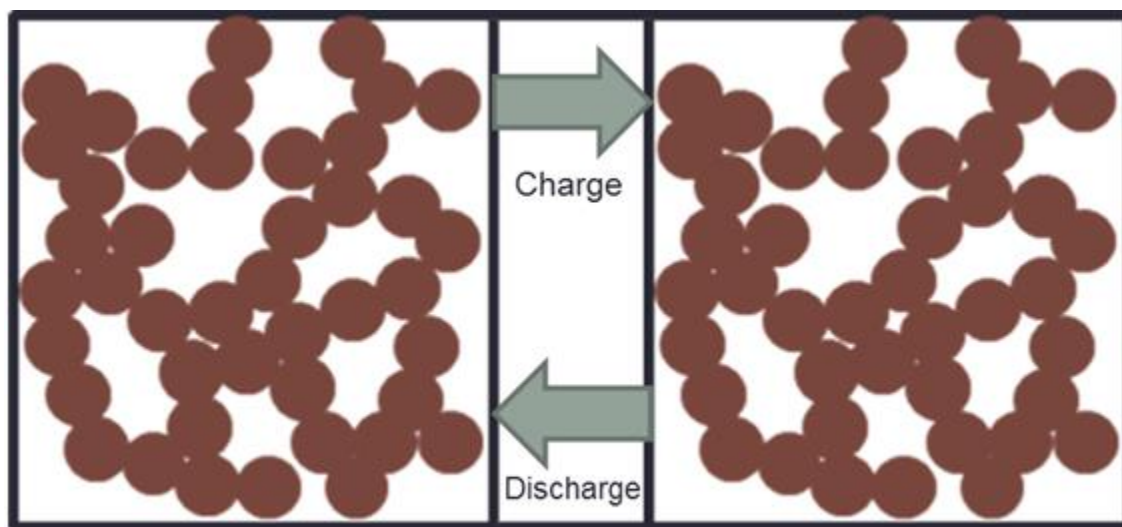
Porous Positive Electrode   **Porous Negative Electrode**

Figure 4.1. Illustration of battery setup. Porous positive electrode separated from the porous negative electrode by an incompressible separator. Electrodes and separator are not shown to scale.
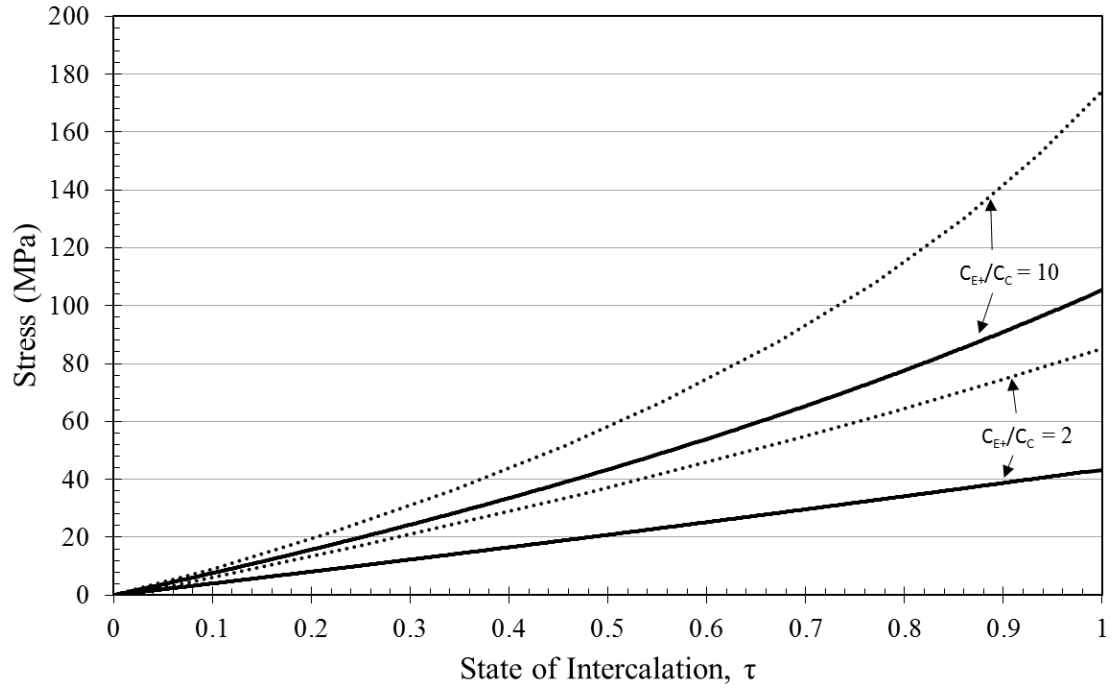
Figure 4.2. Stress generation from single electrode model seen Ref. [1] (dotted lines) compared to stress generation from the two electrode model developed in this work (solid lines). State of intercalation for two electrode model based on the state of intercalation for the expanding electrode.
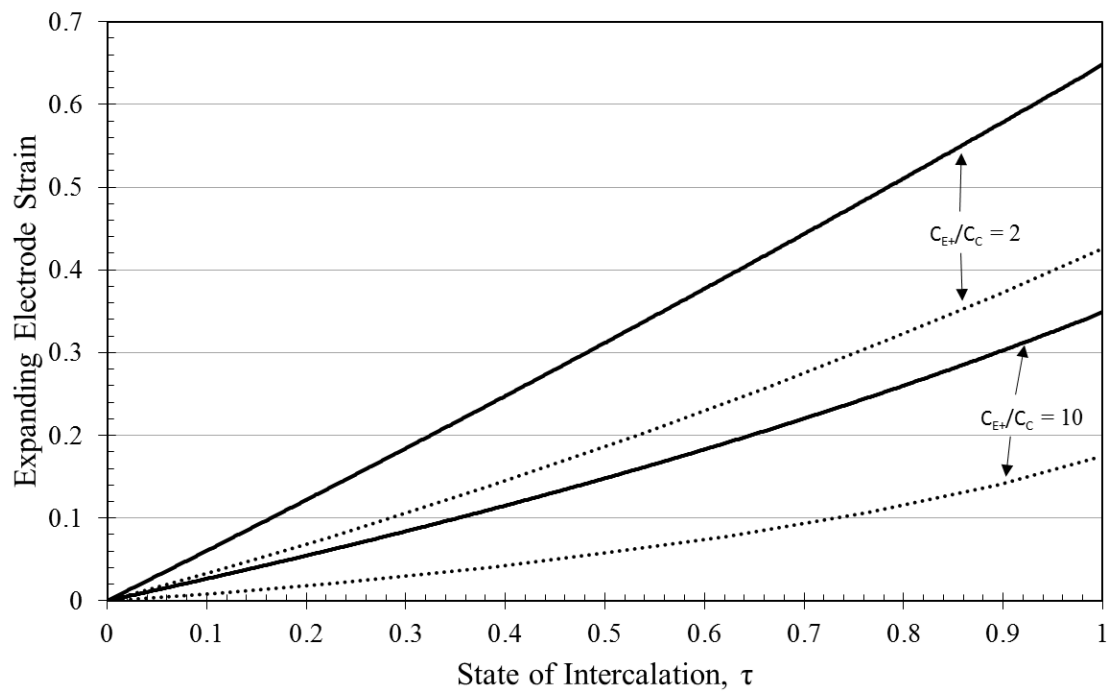
Figure 4.3. Strain development from single electrode model seen in Ref. [1] (dotted lines) compared to strain development in the expanding electrode from the two electrode model in this work (solid lines).
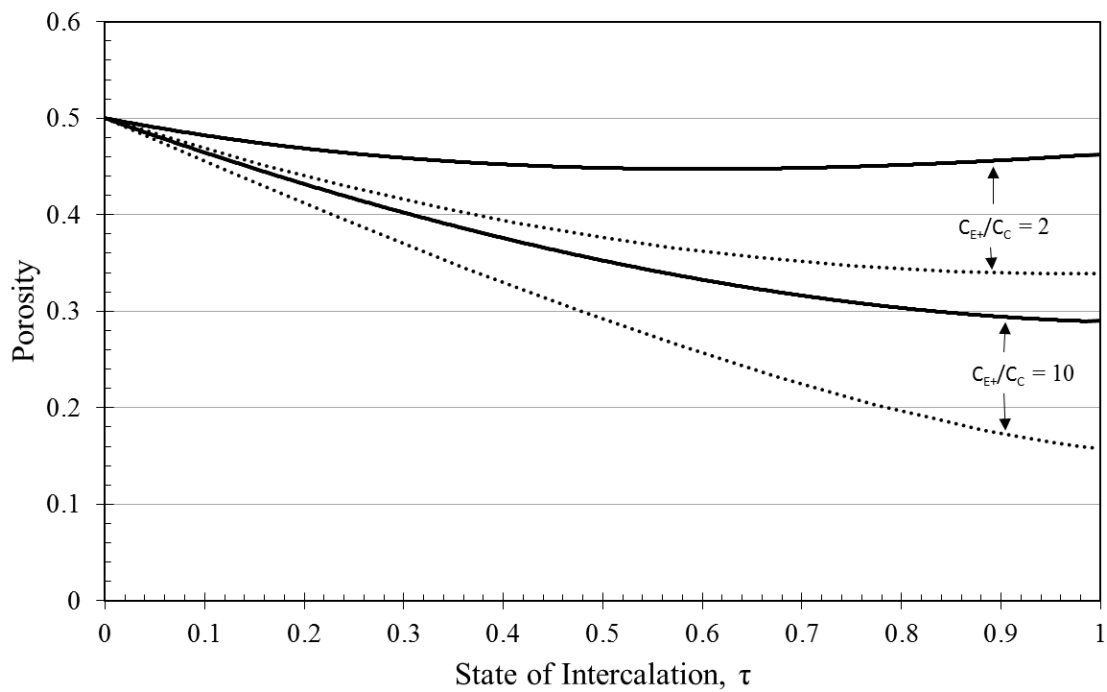
Figure 4.4. Porosity change during intercalation from single electrode model seen in Ref. [1] (dotted lines) compared to porosity development in the expanding electrode from the two electrode model in this work (solid lines).
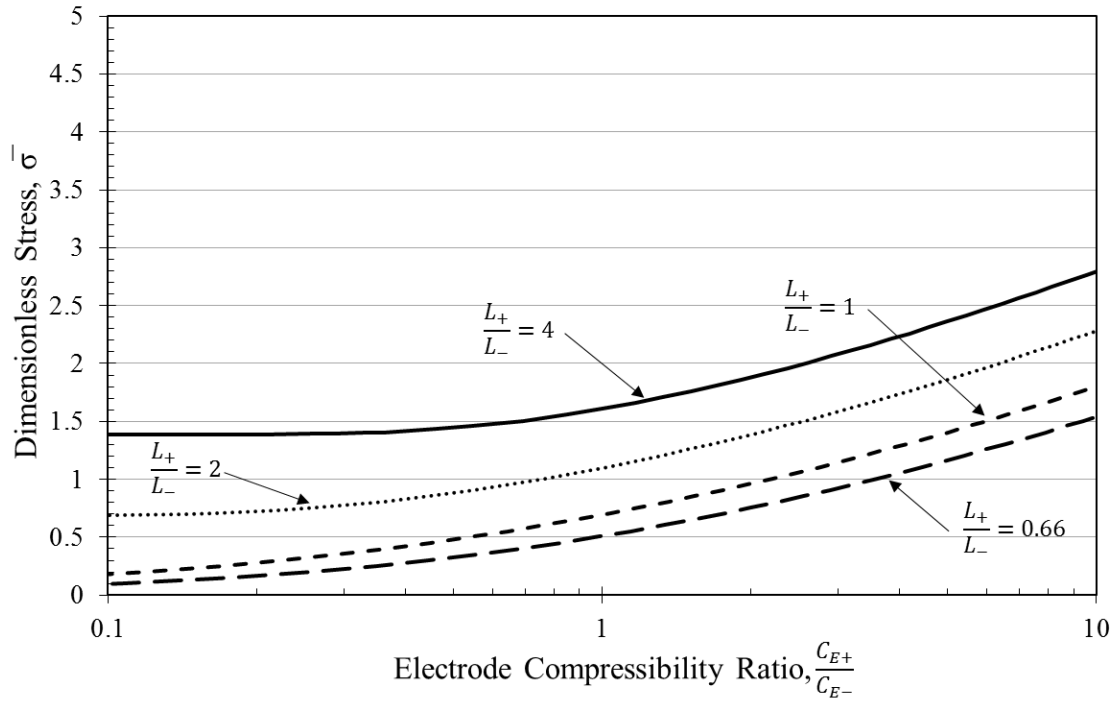
Figure 4.5. Dimensionless stress as a function of the electrode compressibility ratio. L_+ and L_- represent the initial length of the expanding and contracting electrode respectively.
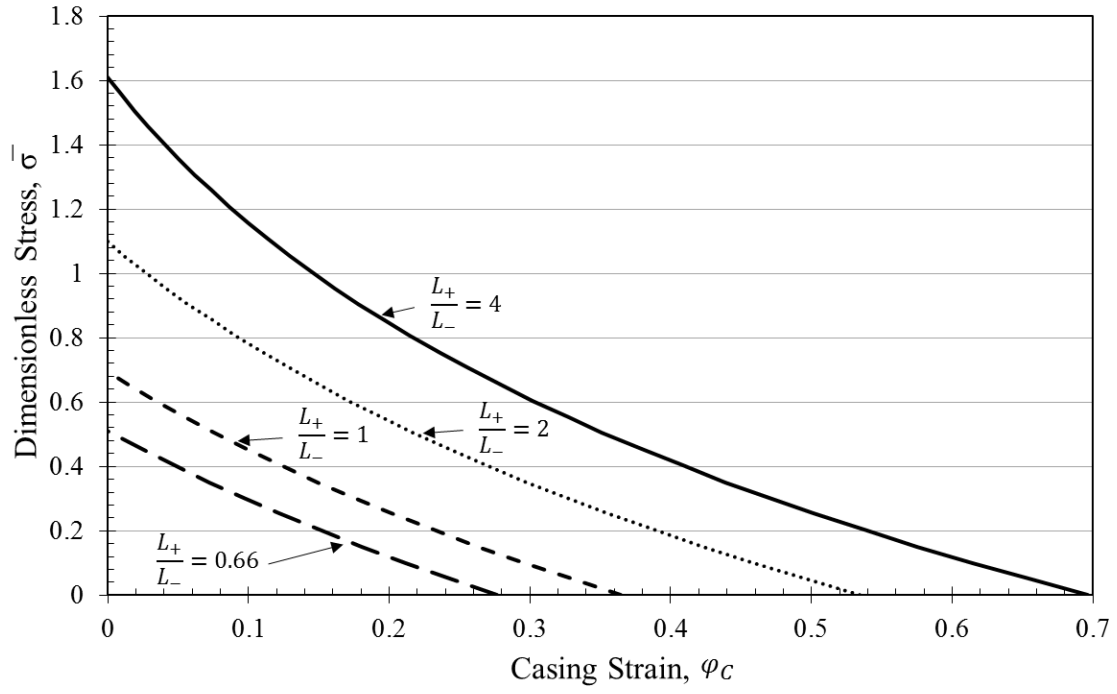
Figure 4.6. Dimensionless stress as a function of the final casing strain. L_+ and L_- represent the initial length of the expanding and contracting electrode respectively.
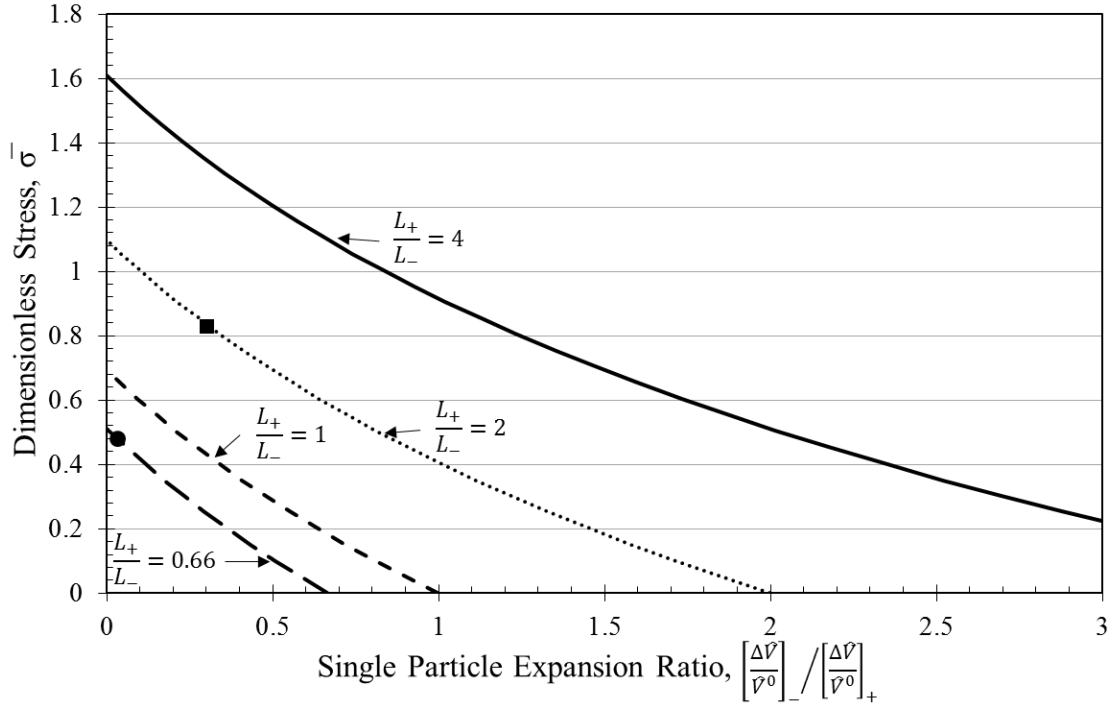
Figure 4.7. Dimensionless stress as a function of the single particle expansion ratio. L_+ and L_- represent the initial length of the expanding and contracting electrode respectively. ■ and ● represent two example cases.
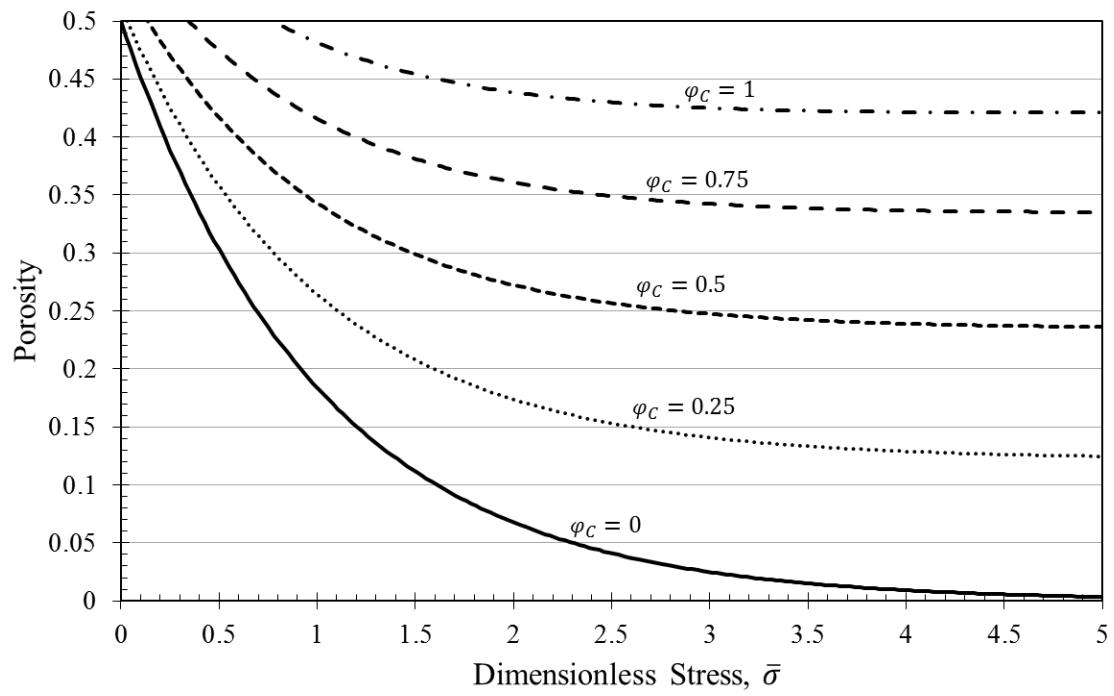
Figure 4.8. Porosity of the expanding electrode at the final state of intercalation as a function of the dimensionless stress in the system. Initial porosity is assumed to be 0.5.

CHAPTER 5

MODELING BATTERY PERFORMANCE DUE TO INTERCALATION DRIVEN VOLUME CHANGE

IN POROUS ELECTRODES

There is an increased focus on improving the range, cost, and fueling times of electric vehicles through the improvement of the design and control of cells[135-144]. New chemistries, such as lithium ion, have also been examined in order to increase the energy densities of these batteries in order to increase the range of battery powered vehicles, and decrease the volume displacement of these batteries in the vehicle powertrain. However, safety problems have arisen in the past several years.[2] Therefore, it is critical to be able to predict the performance of new battery systems in order to improve safety and reliability in alternative energy passenger vehicles while also continuing to increase the energy density.

Newer high capacity anode materials, such as silicon[27, 43-45] and its alloys are receiving much attention due to their significantly higher energy density compared to traditional materials. However, these materials undergo higher volume changes ranging from 100% to 270% during lithiation. Due to the associated challenges presented with these novel materials[1, 43, 78, 146, 147], a modeling approach is necessary to predict the volume change in electrode with active material that undergoes significant expansion. Initially, Gomadam and Weidner[78] developed a model to account for both porosity and dimensional changes and the associated effects on performance, however, they assumed an

64

a priori split between porosity and dimensional changes, rather than directly predicting the volume change.

We recently developed battery models based on rock mechanics that predict the stresses that build up in porous electrodes due to a volume change in the active material during low-rate cycling.[1, 150] These simulations revealed the role that the mechanical properties of the electrodes and battery casing play in the fraction of volume change that goes into porosity changes, and how this fraction varies during the charge and discharge process. However, these earlier models cannot provide insight into how the charge and discharge rate (i.e., current) influences volume change. Here we incorporate the electrodes' stress-strain relationship into a detailed battery model to examine the interplay of porosity and dimensional changes with nonuniform reaction distributions, and ultimately battery performance as a function of rate and electrode properties. The simulations shown here are for a battery comprised of a porous positive electrode, a separator, and a Li foil negative to highlight this interplay.

Model Development

Figure 5.1 shows the setup considered in this work. In order to initially examine non-uniformities in materials undergoing significant volume change, a single porous electrode coupled to a negative lithium reference was used. This is similar to what was seen in earlier studies for a single electrode[1], however, we no longer assume low rate charge or discharge here.

During discharge, charged particle move from the negative lithium electrode through the separator into the positive electrode, resulting in an expansion of the positive

electrode due to an increase in the volume of the active material. A contraction of the positive electrode would be seen during charging.

As given previously[1, 78, 95, 151], the relationship governing the volume change in porous electrodes is obtained from an overall material balance on the solid active material and is seen below:

$$\frac{\partial(1-\varepsilon)}{\partial t} + \nabla \cdot [(1-\varepsilon)\boldsymbol{u}] = -\frac{s\Delta\hat{V}}{nF}j \qquad [1]$$

The term on the right side of the equal sign is the volume change due to intercalating the reacting species into the active material. This volume change can cause either a change in porosity (the first term on the left side of the equal sign) or dimensional changes (second term) expressed by the velocities of the control volume. The velocity vectors can be replaced by the dimensional strain of the electrode, resulting in a simplified version of Equation 1:

$$\frac{\partial(1-\varepsilon)}{\partial t} + \nabla(1-\varepsilon)\cdot\boldsymbol{u} + (1-\varepsilon)\frac{\partial\varphi}{\partial t} = -\frac{s\Delta\hat{V}}{nF}j \qquad [2]$$

If the battery electrodes are anisotropic, unequal expansion in different directions can be included and applied to a more general material balance. Porous rock mechanic theory can be applied in these cases as well. Previous studies[1, 150] neglected the second term in Eq. [2] because porosity was assumed to be uniform across the electrode due to low discharge and charge rates.

As seen in previous works[1], rock mechanics can be used to link volume change in a system with applied pressure through the compressibility of the material under consideration. Here, the compressibility of the electrode undergoing expansion can be treated as a continuum of fractions of the solid phase and pores:

$$C_E = -\frac{1}{V}\frac{dV}{d\sigma} \qquad [3]$$

The volume of the electrode under consideration as a function of strain can be derived from the definition of strain similar to what is seen in solid mechanics, assuming expansion in all directions, or expansion in one direction.

$$V = V^0(1 + \varphi) \tag{4}$$

When solving Equations 3 and 4 simultaneously with the appropriate boundary conditions, the mechanical strain is given a function of electrode compressibility and stress:

$$\varphi_m = e^{-C+\sigma} - 1 \tag{5}$$

If no volume was added to the control volume due to intercalation, this equation would govern the strain of the electrode due to an applied pressure. However, similar to heating in rock mechanics, the control volume expands with the addition of intercalate, and the strain also is a function of the intercalation of ions into the matrix:

$$\varphi_i = \left[\frac{\Delta \hat{V}}{\hat{V}^0}\right]\frac{tI}{Q_{max}} = \left[\frac{\Delta \hat{V}}{\hat{V}^0}\right]\tau \tag{6}$$

For the bulk electrode, τ is defined as a dimensionless time and for the system considered represents the state of intercalation into the positive electrode as well as the state of discharge of the system:

$$\tau = \frac{tI}{Q_{max}} \tag{7}$$

Due to diffusion, the state of intercalation at any point across the electrode could be greater than or less than the overall state of intercalation of the electrode. The strain of the control volume can then be defined by combining Equations 5 and 6:

$$\varphi = \varphi_m + \varphi_i = e^{-C+\sigma} - 1 + \left[\frac{\Delta \hat{V}}{\hat{V}^0}\right]\tau \tag{8}$$

If solving for the strain for the bulk electrode, τ is defined as seen in Equation 7. If solving for the local strain in the electrode, τ is replaced by the local dimensionless lithium concentration in the active material:

$$\theta = \frac{c_p}{c_{max}} \qquad\qquad [9]$$

Equation 8 is the governing equation for the strain at any given position in the electrode based on the state of intercalation at that position if the local dimensionless concentration is used instead of the overall state of cell discharge. The overall strain of the electrode is linked to the strain at each position in the electrode by integrating the local strain across the length of the electrode. With this assumption, solving Equations 7-9 with boundary conditions as seen previously[1, 150] allows for calculation of the stress, local strain, and overall strain in the system. The stress and local strain are used on the left hand side of Equation 2 in order to solve for the porosity in the expanding electrode during discharge. On the right hand side of Equation 2, $\frac{s\Delta\hat{V}}{nF}$ are known parameters based on the system under consideration, leaving j as the final parameter to be calculated.

The equations governing j, the local current density, including equations governing potential in the solid phase, potential in the solution phase, solution phase concentration, active material concentration, and associated boundary conditions are taken from previous works[149] and are reproduced at the end of this chapter. COMSOL Multiphysics® was used to solve the model using a Time Dependent solver set to run until a stop condition of 3.0 V vs Li was reached. The model was one dimensional with respect to voltage, electrolyte concentration, strain, reaction rate, and porosity, and assumed uniformity in the y-direction in Figure 5.1. The concentration of Li in the solid phase was solved in two dimensions, along the length of the electrode, and through the pseudo dimension

representing the radius of a theoretical particle. A parametric sweep was performed to gauge the effect of casing rigidity and discharge rate. The volume expansion of the active material from the discharged to the charged state is 100% (i.e. $\left[\frac{\Delta\hat{V}}{\hat{V}^0}\right] = 1$). This is on the order of magnitude seen in silicon or tin anodes, and is useful for comparison to earlier works.[1]

Results and Discussion

Figure 5.2 illustrates the local strain as a function of dimensionless position in the expanding electrode as a function of dimensionless time and dimensionless position. The separator is located at a dimensionless length of 1, and the current collector is located at a dimensionless length of 0. As seen here, the local strain increases more rapidly closer to the separator primarily due to the rapid reaction of the charged species diffusing to the reaction zone from the separator, reaching a value of 0.6 closest to the separator at the final state of discharge. If the casing was completely compliant, one would expect the maximum strain near the separator to approach 1 due to the results seen in earlier works[1] and the assumption of $\left[\frac{\Delta\hat{V}}{\hat{V}^0}\right] = 1$. However, due to the presence of a moderately rigid casing, the expansion is restricted and does not approach a value of 1. The localized strain is also seen to propagate away from the separator/electrode interface as the active material reaches a high state of intercalation and cannot accept more lithium, and the reactants must then must diffuse further into the electrode to react. The final time shows a significant difference between the strain at each end of the electrode due to the diffusion limitations and concentration gradients present in the system, with a cliff developing between a dimensionless length of 0.5 and 0.6 and showing a change in strain from 0.22 to 0.59. It should be noted that the strain at the separator/electrode interface at the last time step is

69

actually lower than the predicted strain at the time step immediately prior, shown to be 0.06 at a dimensionless time of 0.8, but being compressed close to 0 at the final dimensionless time. This is due to the compression of the electrode by the battery casing associated with the increased stress as discharge progresses and the state of intercalation of ions into the matrix of the positive electrode increases. This phenomenon is also true close to the current collector for the same reasons, and is seen to decrease from 0.64 to 0.6 between the final two time steps.

As mentioned previously, the stress in the system increases as a function of the state of intercalation of charged species into the active material. This stress increase is qualitatively similar to previous works[1] and is not shown here. The rigidity of the battery casing influences the overall stress and strain of the system, and so it follows that a variation in the casing rigidity would also affect the strain distribution in the electrode.

Figure 5.3 illustrates the strain distribution at the end of discharge as the casing rigidity is varied for a constant discharge rate of 1C. The dotted line corresponding to $\frac{C_+}{C_C} = 1$ is the same line seen for $\tau = 1$ in Figure 5.2. $\frac{C_+}{C_C}$ represents the ratio between the compressibility of the expanding electrode compared to the compressibility of the battery casing. For example, a $\frac{C_+}{C_C}$ value of 2 would indicate that the positive electrode is 2 times more compressible than the casing, in other words, the casing is 2 times more rigid than the positive electrode. In Figure 5.3, the strain distribution is similar across all casing rigidities ($\frac{C_+}{C_C}$ values) due to the similarity in diffusion at the same discharge rate, however, the magnitude of the strain across the electrode increases with decreasing casing rigidity due to the increased dimensional changes associated with a more compliant casing. For

$\frac{C_+}{C_C} = 0.1$, the strain close to the separator is 0.92 which is approaching the strain of 1.0 expected for an active material expansion of 100% and a very compliant casing. For $\frac{C_+}{C_C} = 10$, the strain close to the current collector is -0.12 illustrating compression and the effect of increased stress due to the expansion of the active material close to the separator combined with the rigidity of the casing relative to the electrode represented by such a high $\frac{C_+}{C_C}$ value, which decreases the volume change going towards dimensional changes during discharge. The presence of the sharp cliff is also observed between a dimensionless length of 0.5 and 0.6 similar to the last time step seen in Figure 5.2.

Figure 5.4 illustrates the effect of discharge rate on the final strain distribution. Here, the electrode compressibility is held at 2 times the casing compressibility ($\frac{C_+}{C_C} = 2$). The curve corresponding to a 1C discharge rate is identical to the $\frac{C_+}{C_C} = 2$ line in Figure 5.3 and the $\tau = 1$ line seen in Figure 5.2. Here, the C/50 discharge rate is so slow that diffusion limitations are not evident, resulting in a uniform strain distribution of 0.42 at the end of discharge, which shows similar uniformity compared to the cases examined in previous work[1]. As the discharge rate increases, the strain at the end of discharge is seen to be increasingly non-uniform. This is due primarily to diffusion, resulting in a very high reaction rate at the front of the electrode closest to the separator, which manifests in a very non-uniform strain distribution at 10C, and a drop in strain from 0.97 to 0.08 in the area next to the separator. At such high discharge rates, the strain in the active material closest to the separator approaches the 100% expansion assumed for particles in the active material, while the active material close to the current collector has minimal charged particles reach it to intercalate into the matrix, resulting in no positive strain due to the low

stress built up in the system during the lower capacities reached in such high rate discharge. This minimization of charge particles reaching the current collector is also illustrated due to the negative strain observed in the active material closest to the current collector. These results illustrate that the parameter that has the largest effect on the strain distribution in the electrode is the discharge rate when compared to the varying casing rigidity seen in Figure 5.3.

Figure 5.5 illustrates the change in average porosity for the electrode under consideration as a function of state of discharge. Coupling the local strain predictions with the bulk stress predictions allows for the prediction of porosity distributions across the thickness of the electrode, and in turn allows for predictions of the average electrode porosity. The prediction of the average electrode porosity can be compared to the uniform model detailed previously[1, 150] and the model seen in this work. Here, it can be seen that increasing the rigidity of the casing while the rigidity of the electrode remains constant (increasing $\frac{C_+}{C_C}$) results in a decrease in the porosity as discharge progresses. This is due to the volume change being forced into porosity changes instead of dimensional changes due to the increase in bulk stress during discharge. When considering a relatively compliant casing ($\frac{C_+}{C_C} = 0.1$), the volume change goes more towards dimensional changes than porosity changes, resulting in a higher predicted final porosity of 0.33 for the system. A rigid casing ($\frac{C_+}{C_C} = 10$) forces more volume changes into dimensional changes and results in the system reaching the cutoff voltage at a dimensionless discharge capacity of 0.9 and a porosity of 0.27 even at very low discharge rates. The final average porosity seen in the electrode is only a function of the state of discharge and the overall predicted stress,

72

however, the distribution of the porosity in the system is a function of the discharge rate due to the presence of strain distributions in the system.

Figure 5.6 illustrates the development of porosity gradients as a function of state of discharge across the dimensionless length of the electrode. The porosity distributions seen here are predicted through the use of Equation 5.2. Here, the strain distributions are coupled with the stress and substituted into the unknowns in Equation 5.2. The porosity is uniform across the electrode at the beginning of discharge, initially at 0.492. As discharge progresses, the porosity becomes more non-uniform due to a 1C discharge rate and the associated localized strain, with lower porosities predicted closer to the separator. This is due to the higher localized strain predicted close to the separator combined with the increased stress in the system. At the final state of discharge, the porosity is seen to be the most non-uniform with higher porosities close to 0.39 predicted closer to the current collector and a porosity of 0.308 predicted close to the separator. The strain at the current collector is low at the end of discharge, and the porosity change during discharge is high due to the bulk stresses generated in the system associated with a casing that is 2 times more rigid than the electrode, illustrating the split between volume changes going towards dimensional changes as seen by the strain distributions in earlier figures compared to the porosity changes seen in Figure 5.6.

Figure 5.7 illustrates the porosity at the end of discharge for a 1C rate under varying casing rigidities corresponding to the strain profiles seen earlier in Figure 5.3. Here, the $\frac{c_+}{c_c}$ values are identical to those seen in the stress and strain figures shown earlier. Similar porosity distributions are predicted as the casing rigidity varies with the overall magnitude of the porosity decreasing as the casing rigidity is increased. This is due to more volume

changes going into porosity changes instead of dimensional changes with the presence of a more rigid casing. Regardless of the casing rigidity, it is seen that the porosity is low close to the separator, and high close to the current collector. This is due to the diffusion limitations and associated strain distributions across the length of the electrode. For a more compliant casing ($\frac{C_+}{C_C} = 0.1$), the porosity close to the separator is 0.32. Increasing the rigidity of the casing by two orders of magnitude ($\frac{C_+}{C_C} = 10$) results in a decrease in the porosity to 0.298 close to the separator at the end of discharge. The variation of porosity distributions with rigidity are expected to have an effect on the overall resistance of the electrode and associated losses during discharge, which will illustrate the effect of casing rigidity and varying stresses on the system and the effect of the porosity distribution in the electrode.

Figure 5.8 illustrates the porosity at the end of discharge for different rates. Similar to the strain distributions, the porosity distributions are also seen to be affected by the discharge rate, and in turn the state of discharge. The end of discharge was assumed to be when the system reached 3V, resulting in the highest discharge capacity being realized for low discharge rates, and the lowest discharged capacity being realized for the 10C rate. Therefore, the amount of volume changes going towards either porosity changes or dimensional changes is maximized for low discharge rates. Similar to the strain distribution, when the system undergoes discharge at a low rate, the system is not diffusion limited which results in a uniform porosity distribution of 0.282 at the end of discharge. Higher rates of discharge result in more non-uniform porosity distributions. The changes in the porosity distributions significantly affect the local reaction rate as well as the rate of diffusion of charged particles from the separator towards the current collector. Due to the

highest discharge capacity being realized under a low discharge rate, the lowest porosity is seen to be at the C/50 rate, with final porosities increasing as the discharge rate increases. The development of these non-uniformities in porosity affect the diffusion of reactants through the electrode, resulting in losses in the overall voltage due to changes in the local reaction rate.

Figure 5.9 shows the localized reaction rate distribution for a 1C discharge with a battery constrained with a casing that is 2 times more rigid than the expanding electrode. Here, it can be seen that as the state of discharge increases, the reaction rate becomes more non-uniform with a reaction front appearing towards the alter stages of discharge and propagating from the separator towards the current collector. Initially, the local reaction rate increases rapidly close to the separator and reaches a maximum of 1 mA/cm^3. This peak shifts towards the current collector and rapidly increases from 2 mA/cm^3 to 8.8 mA/cm^3 across the last few time steps. At the final state of discharge, it is seen that the reaction rate is the most non-uniform with the peak located around 0.58 located at the same place that the large non-uniformity in strain is seen in Figure 5.3 and Figure 5.2. This results in a mass transfer limited situation due to the lithium particles diffusing through the low porosity regions until they reach the regions with lower strain (lower intercalation state) and react, causing significant voltage losses contributing to the lowering of realized discharge capacity when increasing the discharge rate. This high localized reaction rate contributes to the large changes in porosity and strain due to the immediate intercalation of diffusing reactants once they reach this high rate region.

Figure 5.10 illustrates the discharge for the theoretical system modeled here through the combination of the porosity changes, strain changes, stress, concentration

distributions, and reaction distributions. The potential seen here is a function of dimensionless discharge capacity for three different rates. A dimensionless discharge capacity of 1 is the theoretical maximum discharge capacity based on the maximum theoretical capacity of the positive electrode. The equilibrium potential used here is for a lithium nickel manganese cobalt oxide electrode and mechanical properties were selected that are similar to those seen in electrode materials undergoing high expansion. Selecting one discharge capacity, such as C/2, shows that increasing the rigidity of the casing with respect to the electrode compressibility results in a net loss of discharge capacity. For a C/2 rate, a system with a $\frac{C_+}{C_C}$ value of 0.1 is predicted to have a discharge capacity close to the theoretical maximum. Increasing the $\frac{C_+}{C_C}$ value by two orders of magnitude shows a 20% loss in realized capacity. This is due to the decrease in porosity seen earlier and the associated increase in ionic resistance and diffusion limitations. When the discharge rate is increased, the effect of non-uniform porosity and diffusion limitations is further enhanced. When examining a 1C discharge in a system where $\frac{C_+}{C_C} = 0.1$ shows a realized capacity of 68% of the theoretical maximum. Increasing the casing rigidity also shows a decrease in realized capacity, to approximately 62%. Finally, increasing the discharge rate to 2C shows a realized capacity of less than 40% of the theoretical maximum regardless of the casing rigidity. For this figure, the equilibrium potential was chosen for simplicity, however, any initial porosity and equilibrium equations can be used with this treatment.

The effect of discharge rate on a system with high expansion in the active material is significant. Here we show the cell potential as a function of dimensionless discharge capacity for a $\frac{C_+}{C_C}$ of 2 and a range of discharge rates. This illustrates the large effect that

volume change can have on the available capacity in the battery. Here we see that enabling the electrode to undergo dimensional changes while attempting to lessen the volume change that goes towards porosity change would prove useful to realizing a higher discharge capacity due to the decrease diffusion resistance in the electrode. This increase of dimensional changes could be realized through the use of a casing that is less rigid than the electrode, such as the case of a pouch cell, as well as using a secondary electrode that has a high single particle expansion that contracts during discharge, lessening the generated stresses and allowing for greater dimensional changes in the expanding electrode.

Conclusion

The objective here was to extend the modeling approach using porous rock mechanics coupled with porous electrode theory to predict the dimensional and porosity changes in a porous electrode caused by volume change in the active material during intercalation without the assumption of uniformity in concentration, porosity, or reaction rate. This serves to predict the local phenomena present in an electrode undergoing significant volume expansion at high rates. The effect of splitting volume change into porosity and dimensional changes is seen to affect the porosity and strain distributions across the electrode thickness. Finally, the porosity and porosity distributions were used to predict concentration gradients, which was in turn used to predict the associated drop in performance based on the resistance to electrode expansion and discharge rate. This approach can be coupled with experimentally determined material characteristics to predict and account for volume change in real systems in future work.

Additional Equations

Potential in the Positive Electrode Solid Phase

$$\frac{\partial}{\partial x}\left[-\frac{\sigma_{eff}}{L}\frac{\partial \emptyset_1}{\partial x}\right] = -S_a i_n L \qquad \text{Governing Equation} \qquad \text{[A1.1]}$$

$$-\frac{\sigma_{eff}}{L}\frac{\partial \emptyset_1}{\partial x} = 0 \qquad \text{BC at separator interface} \qquad \text{[A1.2]}$$

$$-\frac{\sigma_{eff}}{L}\frac{\partial \emptyset_1}{\partial x} = i_{app} \qquad \text{BC at positive current collector} \qquad \text{[A1.3]}$$

$$\emptyset_1 = \emptyset_1^{initial} \qquad \text{Initial Value} \qquad \text{[A1.4]}$$

Potential in the Positive Electrode Solution Phase

$$\frac{\partial}{\partial x}\left[-\frac{\kappa_{eff}}{L}\frac{\partial \emptyset_2}{\partial x} + \frac{\kappa_{effd}}{Lc_2}\frac{\partial c_2}{\partial x}\right] = -S_a i_n L \qquad \text{Governing Equation} \qquad \text{[A2.1]}$$

$$-\frac{\kappa_{eff}}{L}\frac{\partial \emptyset_2}{\partial x} + \frac{\kappa_{effd}}{Lc_2}\frac{\partial c_2}{\partial x} = 0 \qquad \text{BC at positive current collector} \qquad \text{[A2.2]}$$

$$\emptyset_2|^{pos} = \emptyset_2|^{sep} \qquad \text{BC at separator interface} \qquad \text{[A2.3]}$$

$$\emptyset_2 = \emptyset_2^{initial} \qquad \text{Initial Value} \qquad \text{[A2.4]}$$

Positive Electrode Solution Phase Concentration

$$\frac{\partial}{\partial x}\left[-\frac{D_{2,eff}}{L}\frac{\partial c_2}{\partial x}\right] = \frac{1-t_+}{F}S_a i_n L \qquad \text{Governing Equation} \qquad \text{[A3.1]}$$

$$-\frac{D_{2,eff}}{L}\frac{\partial c_2}{\partial x} = 0 \qquad \text{BC at positive current collector} \qquad \text{[A3.2]}$$

$$c_2|^{pos} = c_2|^{sep} \qquad \text{BC at separator interface} \qquad \text{[A3.3]}$$

$$c_2 = c_2^{initial} \qquad \text{Initial Value} \qquad \text{[A3.4]}$$

Separator Region Solution Phase Potential

$$\frac{\partial}{\partial x}\left[-\frac{\kappa_{eff}}{L}\frac{\partial \emptyset_2}{\partial x} + \frac{\kappa_{effd}}{Lc_2}\frac{\partial c_2}{\partial x}\right] = 0 \qquad \text{Governing Equation} \qquad \text{[A4.1]}$$

$$\emptyset_2|^{pos} = \emptyset_2|^{sep} \qquad \text{BC at positive electrode interface} \qquad \text{[A4.2]}$$

$$\emptyset_2|^{sep} = 0 \qquad \text{BC at negative electrode interface} \qquad \text{[A4.3]}$$

$$\emptyset_2|^{sep} = \emptyset_2^{initial} \qquad \text{Initial Value} \qquad \text{[A4.4]}$$

Negative Electrode Reference Potential

$$\emptyset_1^{negative} = -\frac{2RT}{F}\sinh^{-1}\left(\frac{i_{app}}{2k_0 F\sqrt{c_2}}\frac{A_{neg}}{A_{pos}}\right) \qquad \text{Governing Equation} \qquad [A5.1]$$

Separator Region Solution Phase Concentration

$$\frac{\partial}{\partial x}\left[-\frac{D_{2,eff}}{L}\frac{\partial c_2}{\partial x}\right] = 0 \qquad \text{Governing Equation} \qquad [A6.1]$$

$$c_2|^{pos} = c_2|^{sep} \qquad \text{BC at positive electrode interface} \qquad [A6.2]$$

$$-\frac{D_{2,eff}}{L}\frac{\partial c_2}{\partial x} = i_{app}\left(\frac{1-t_+}{F}\right) \qquad \text{BC at negative electrode interface} \qquad [A6.3]$$

$$c_2 = c_2^{initial} \qquad \text{Initial Value} \qquad [A6.4]$$

Pseudo Two Dimensional Model for Particle Region Concentration

$$y^2 r_p \frac{\partial c_1}{\partial t} + \frac{\partial}{\partial x}\left[-\frac{\varepsilon x^2 D_{Li}}{r_p}\frac{\partial c_1}{\partial x}\right] + \frac{\partial}{\partial y}\left[-\frac{y^2 D_{Li}}{r_p}\frac{\partial c_1}{\partial y}\right] = 0 \quad \text{Governing Equation} \qquad [A7.1]$$

$$-\frac{\varepsilon x^2 D_{Li}}{r_p}\frac{\partial c_1}{\partial x} = 0 \qquad \text{BC at positive current collector} \qquad [A7.2]$$

$$\frac{\varepsilon x^2 D_{Li}}{r_p}\frac{\partial c_1}{\partial x} = 0 \qquad \text{BC at separator} \qquad [A7.3]$$

$$-\frac{y^2 D_{Li}}{r_p}\frac{\partial c_1}{\partial x} = 0 \qquad \text{BC at } y = 0 \qquad [A7.4]$$

$$\frac{y^2 D_{Li}}{r_p}\frac{\partial c_1}{\partial x} = -\frac{i_n}{F} \qquad \text{BC at } y = 1 \qquad [A7.5]$$

$$c_1 = c_1^{initial} \qquad \text{Initial Value} \qquad [A7.6]$$

Boundary Equations for Active Material and Electrolyte Interface

$$i_n = i_0\left[\exp\left(\frac{\eta\alpha_a F}{RT}\right) - \exp\left(-\frac{\eta\alpha_a F}{RT}\right)\right] \qquad \text{Butler-Volmer Equation} \qquad [A8.1]$$

$$i_0 = k_0 F\left(c_{1,max} - c_{1,s}\right)^{\alpha_a} c_2^{\alpha_c} c_{1,s}^{\alpha_c} \qquad \text{Exchange current density} \qquad [A8.2]$$

$$\eta = \emptyset_1 - \emptyset_2 - U_{eq} \qquad \text{Overpotential} \qquad [A8.3]$$

Symbols

φ	Electrode Strain
ε	Porosity
ε^0	Initial Porosity
t	Time, s
$\boldsymbol{u}$	Electrode velocity, m/s
s	Stoichiometric reaction coefficient
$\hat{V}$	Molar volume, cm^3/mol
n	Electrons transferred in the reaction
F	Faraday's constant, 96485 C/mol
j	Current density, A/cm^3
x	Dimension along the electrode length
V	Volume of the electrode, cm^3
C_+	Electrode compressibility, 1/GPa
C_C	Casing compressibility, GPa^{-1}
σ	Stress, GPa
V^0	Initial electrode volume, cm3
φ_m	Mechanical strain
φ_i	Intercalation strain
$\hat{V}^0$	Initial molar volume of active material, cm3/mol
τ	State of intercalation
I	Bulk applied current
Q_{max}	Maximum capacity of the electrode, C

σ_{eff} Effective conductivity of solid phase, S/cm

$\emptyset_1$ Potential in solid phase, V

L Electrode length

S_a Specific surface area of electrode, m-1

i_n Current density at interface, A/cm2

i_{app} Applied current density, A/cm2

$\emptyset_1^{initial}$ Initial solid phase potential, V

κ_{eff} Solution phase effective conductivity, S/cm

$\emptyset_2$ Potential in the solution phase, V

c_2 Solution phase concentration, mol/cm3

κ_{effd} Modified effective solution phase conductivity, S/cm

$\emptyset_2|^{pos}$ Solution phase potential at the positive electrode interface, V

$\emptyset_2|^{sep}$ Solution phase potential at the separator interface, V

$\emptyset_2^{initial}$ Initial solution phase potential

$D_{2,eff}$ Effective diffusion coefficient

t_+ Transfer Coefficient

$c_2|^{pos}$ Solution phase concentration at the positive electrode interface, mol/cm3

$c_2|^{sep}$ Solution phase concentration at the separator interface, mol/cm3

$c_2^{initial}$ Initial solution phase concentration, mol/cm3

κ_{effd} Modified solution phase effective conductivity, S/cm

$\emptyset_1^{negative}$ Negative electrode solid phase potential

R Gas constant, J/mol/K

T Temperature

A_{neg} Area of negative electrode at current collector, cm2

A_{pos} Area of positive electrode at current collector, cm2

k_0 Reaction rate constant

$D_{2,eff}$ Effective diffusion coefficient in separator

c_1 Solid phase concentration in active material particle, mol/cm3

D_{Li} Diffusion coefficient for Li in particle

r_p Radius of particle, m

$c_1^{initial}$ Initial solid phase concentration, mol/m3

c_1^{max} Maximum solid phase concentration, mol/m3

i_0 Exchange current density, A/cm2

η Overpotential, V

U_{eq} Equilibrium potential, V

α_a Anodic transfer coefficient

α_c Cathodic transfer coefficient

Table 5.1 Constants

Parameter	Value	Reference
C_C	Varies	[1, 95, 150]
C_E	0.43 1/GPa	
ε^0	0.49167	[42, 43]
T	298 K	[149]
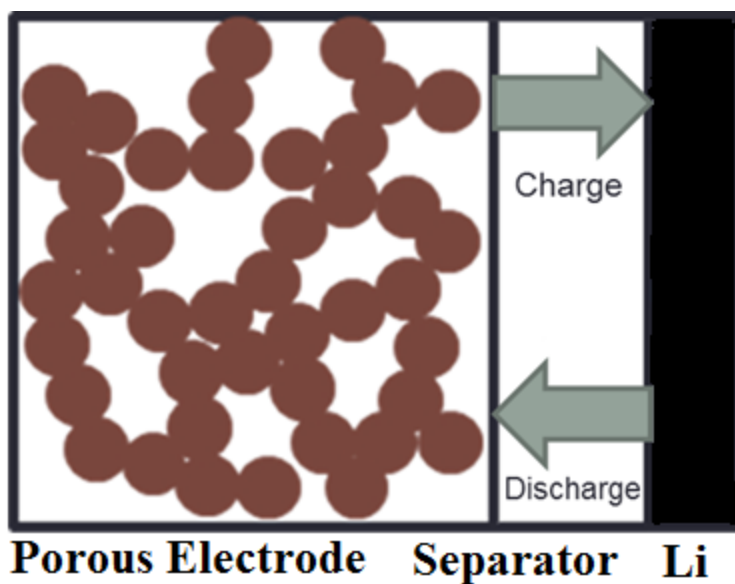
Figure 5.1. A schematic of the battery system modeled here. It involves a porous positive electrode, a separator, and a Li foil negative. The dark circles in the porous electrode represents the active intercalation material and the white space is the electrolyte. This schematic is not shown to scale.
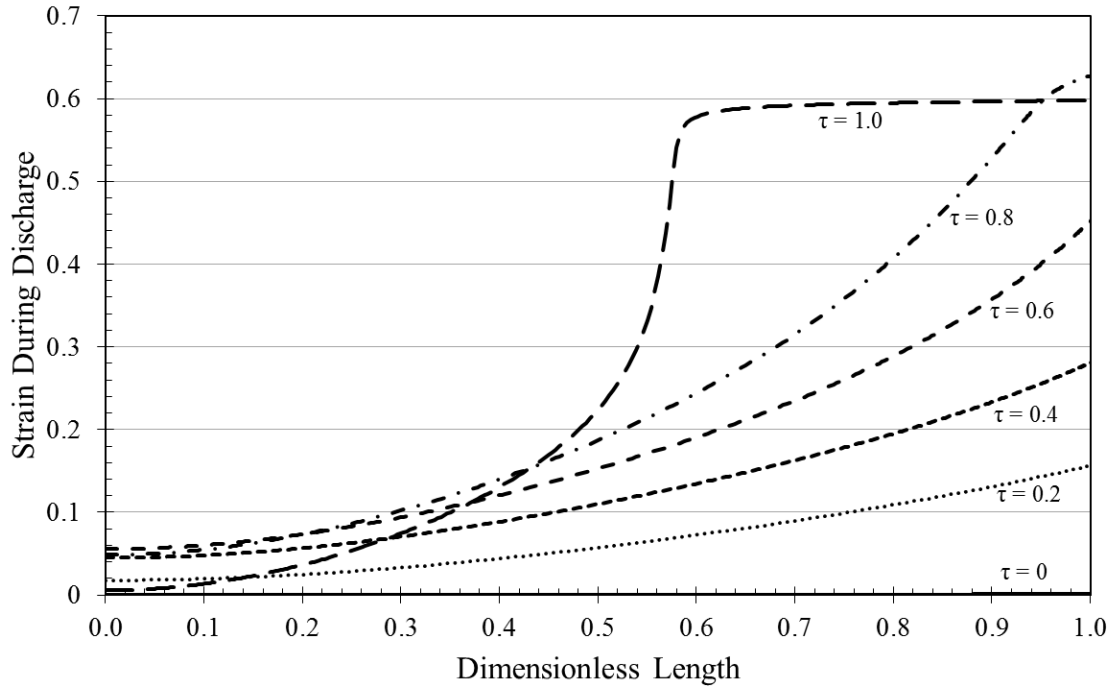
Figure 5.2. Strain distribution during discharge. $\frac{C_+}{C_C}$ is 2 indicating a casing that is 2 times as rigid as the electrode undergoing expansion. Rate is 1C. Discharge interval is 1/5 of overall discharge obtained at the 1C rate. Single particle expansion is 100%.
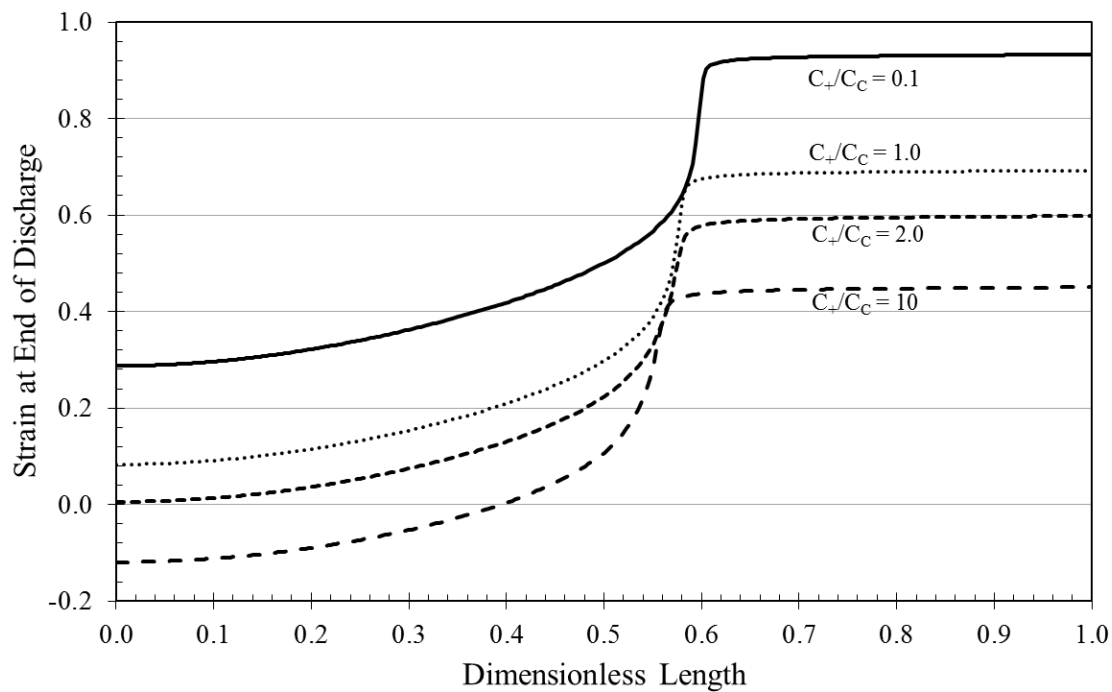
Figure 5.3. Strain distribution at the end of discharge as a function of dimensionless length and $\frac{c_+}{c_C}$. Four different values of $\frac{c_+}{c_C}$: 0.1, 1, 2, 10. Discharge rate is 1C. Positive electrode single particle expansion during intercalation is 100%.
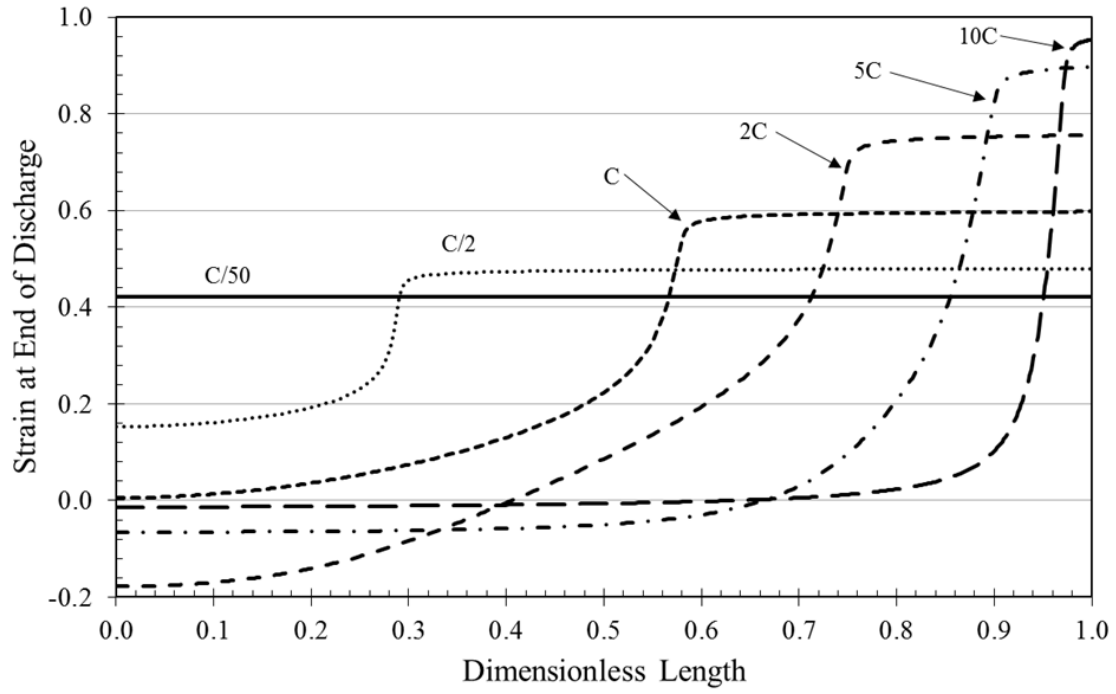
Figure 5.4. Strain distribution at the end of discharge as a function of dimensionless length and discharge rate. Many different discharge rates are shown here. From right to left: C/50, C/2, C, 2C, 5C, 10C. Positive electrode single particle expansion during intercalation is 100%. $\frac{c_+}{c_C}$ is 2.
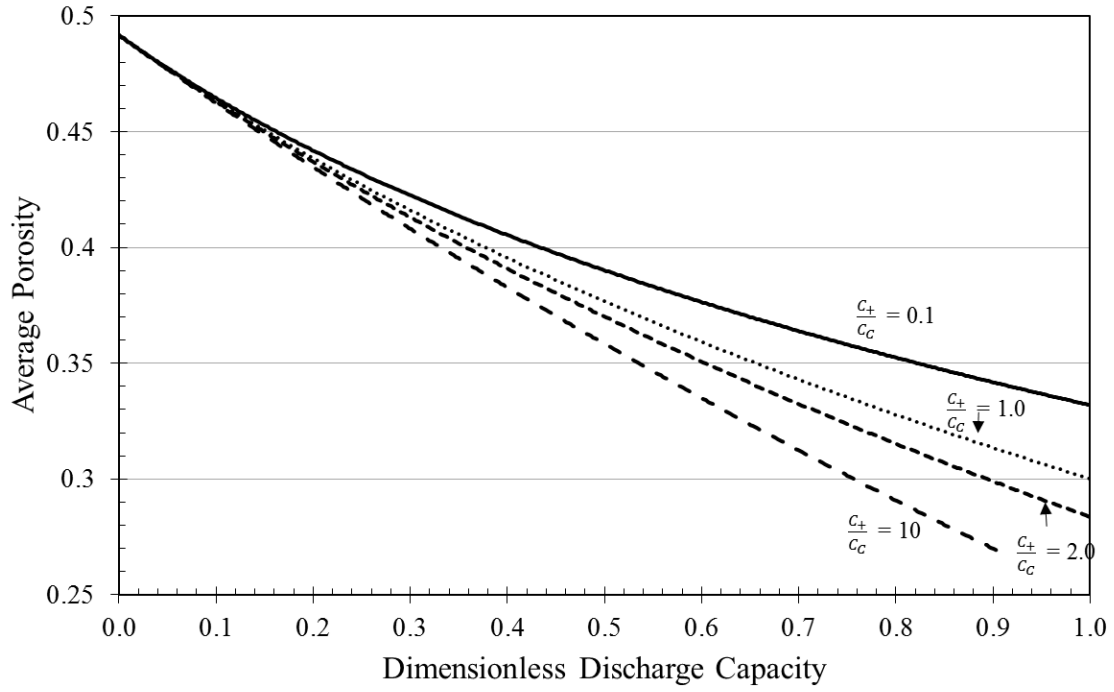
Figure 5.5. Overall porosity of the electrode as a function of dimensionless discharge capacity. The only difference between discharge rates is the point at which discharge ceases. The relative rigidity of the casing material compared to the positive electrode under consideration varies ($\frac{C_+}{C_C}$ values of 0.1, 1, 2, and 10). The positive electrode single particle expansion during intercalation is 100%.
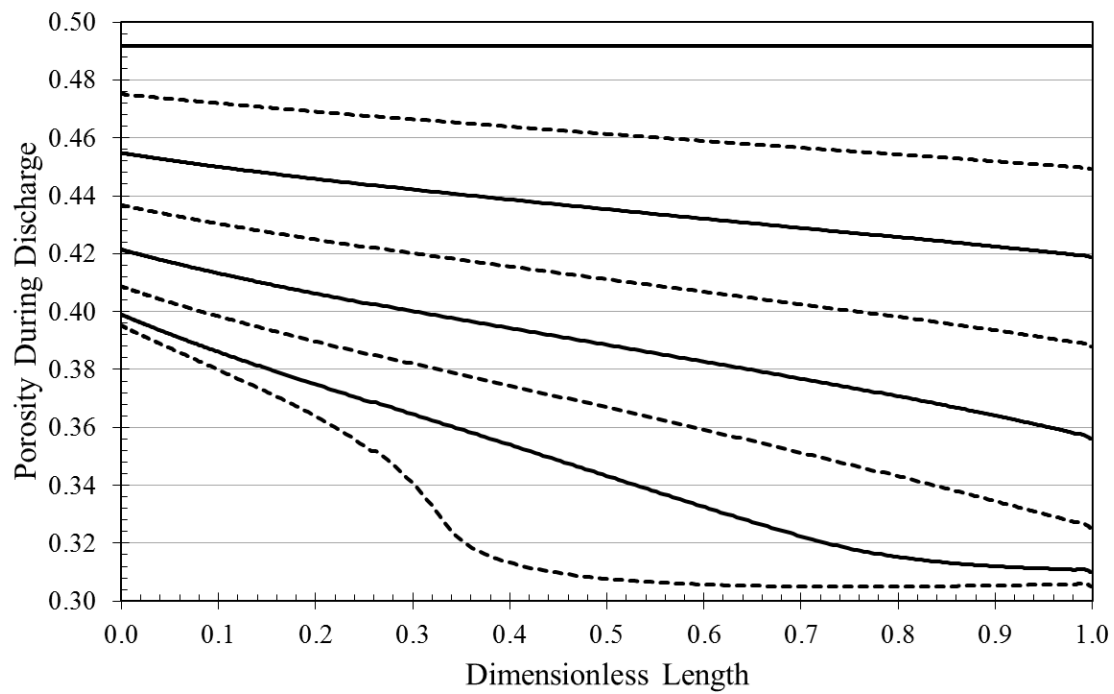
Figure 5.6. Porosity during discharge at a 1C discharge rate and $\frac{c_+}{c_c}$ of 2. Single particle expansion is 100%.
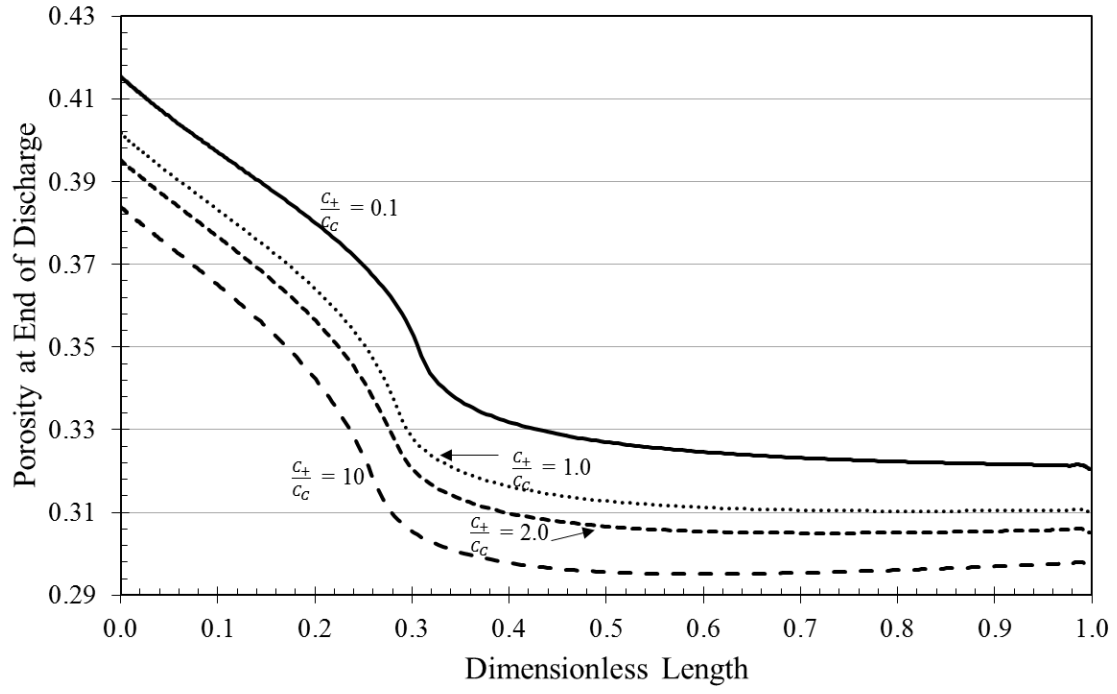
Figure 5.7. Porosity at the end of discharge at 1C discharge rate for four different$\frac{C_+}{C_C}$: 0.1, 1, 2, 10. Single particle expansion is 100%.
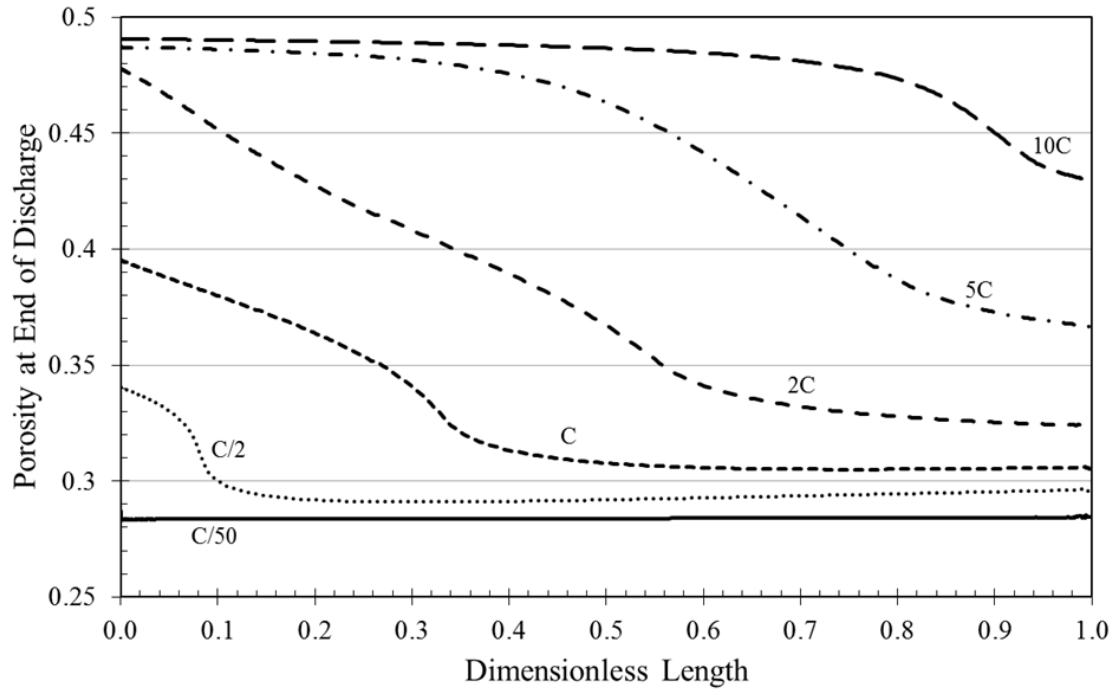
Figure 5.8. Porosity at the end of discharge for different rates: C/50, C/2, C, 2C, 5C, 10C. $\frac{c_+}{c_c}$ is 2. Single particle expansion is 100%.
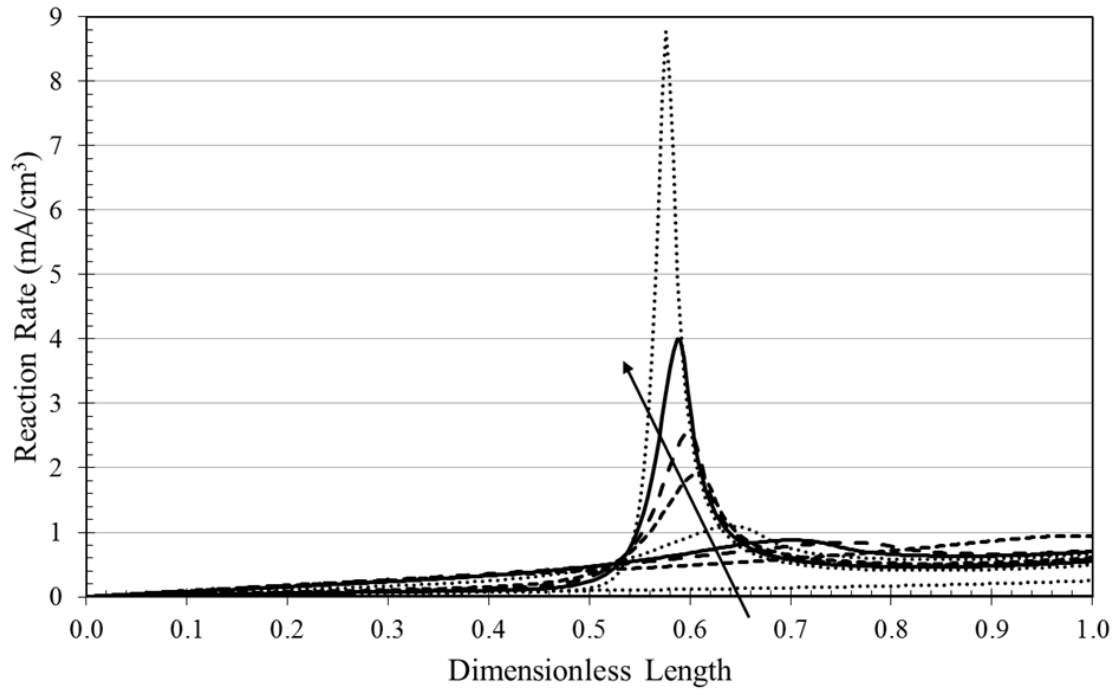
Figure 5.9. Reaction Distribution in the expanding electrode during discharge. $\frac{c_+}{c_c}$ is 2 and the single particle expansion is 100%.
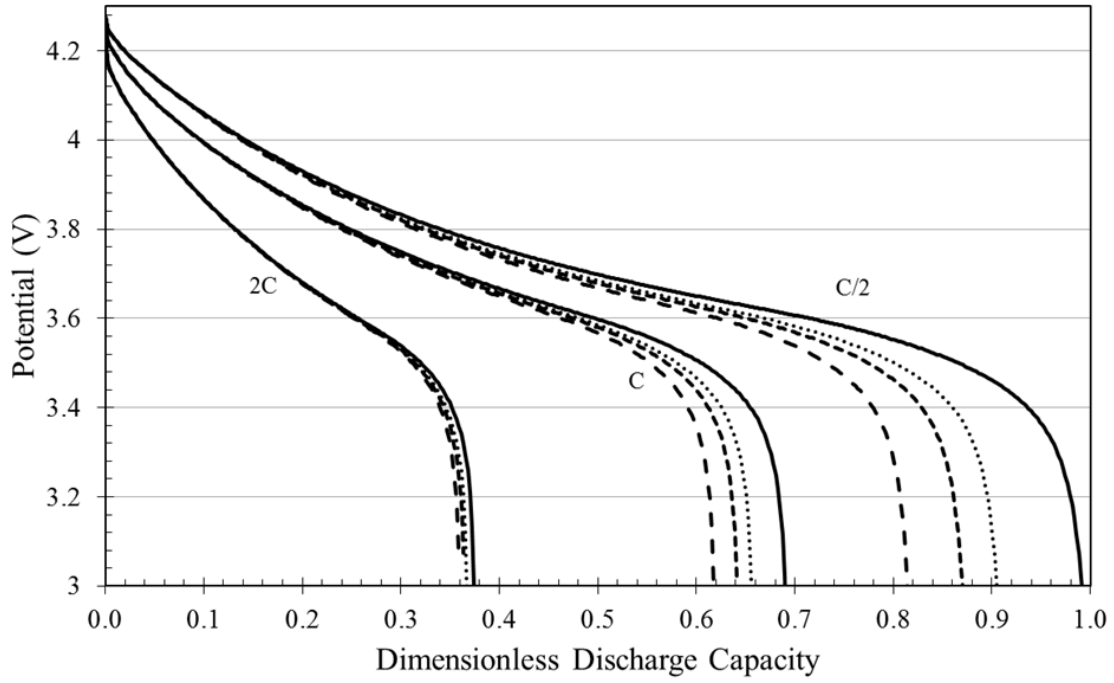
Figure 5.10. Cell potential as a function of dimensionless discharge capacity for 3 different discharge rates (C/2, C, and 2C) illustrating the effect of changing the rigidity of the casing material relative to the rigidity of the positive electrode under consideration (0.1, 1, 2, 10 $\frac{C_+}{C_C}$ values). Positive electrode single particle expansion during intercalation is 100%.

REFERENCES

1. T. R. Garrick, K. Kanneganti, X. Y. Huang and J. W. Weidner, *J Electrochem Soc*, **161**, E3297 (2014).

2. N. Williard, W. He, C. Hendricks and M. Pecht, *Energies*, **6**, 4682 (2013).

3. S. Wilke, B. Schweitzer, S. Khateeb and S. Al-Hallaj, *J Power Sources*, **340**, 51 (2017).

4. Q. Wang, P. Ping, X. Zhao, G. Chu, J. Sun and C. Chen, *J Power Sources*, **208**, 210 (2012).

5. A. Hammami, N. Raymond and M. Armand, *Nature*, **424**, 635 (2003).

6. P. Balakrishnan, R. Ramesh and T. P. Kumar, *J Power Sources*, **155**, 401 (2006).

7. R. Petibon, V. L. Chevrier, C. P. Aiken, D. S. Hall, S. R. Hyatt, R. Shunmugasundaram and J. R. Dahn, *J Electrochem Soc*, **163**, A1146 (2016).

8. Q. Zhang, Q. Z. Guo and R. E. White, *J Power Sources*, **165**, 427 (2007).

9. Q. Zhang and R. E. White, *J Electrochem Soc*, **154**, A587 (2007).

10. T. Ohzuku, A. Ueda, M. Nagayama, Y. Iwakoshi and H. Komori, *Electrochim Acta*, **38**, 1159 (1993).

11. H. Wang, Y. I. Jang, B. Huang, D. R. Sadoway and Y. M. Chiang, *J Electrochem Soc*, **146**, 473 (1999).

12. Y. T. Zheng, X. J. Hao, J. M. Niu and B. W. Pan, *Mater Lett*, **163**, 98 (2016).

13. A. R. Armstrong and P. G. Bruce, *Nature*, **381**, 499 (1996).

14. F. Capitaine, P. Gravereau and C. Delmas, *Solid State Ionics*, **89**, 197 (1996).

15. J. Reimers, E. W. Fuller, E. Rossen and J. Dahn, *J Electrochem Soc*, **140**, 3396 (1993).

16. J. Y. Ji, J. L. Liu, L. F. Lai, X. Zhao, Y. D. Zhen, J. Y. Lin, Y. W. Zhu, H. X. Ji, L. L. Zhang and R. S. Ruoff, *Acs Nano*, **9**, 8609 (2015).

17. P. Keil, S. F. Schuster, J. Wilhelm, J. Travi, A. Hauser, R. C. Karl and A. Jossen, *J Electrochem Soc*, **163**, A1872 (2016).

18. E. Markevich, G. Salitra and D. Aurbach, *J Electrochem Soc*, **163**, A2407 (2016).

19. V. P. Nemani, S. J. Harris and K. C. Smith, *J Electrochem Soc*, **162**, A1415 (2015).

20. V. R. Subramanian, P. Yu, B. N. Popov and R. E. White, *Elec Soc S*, **2000**, 124 (2004).

21. P. Yu, J. A. Ritter, R. E. White and B. N. Popov, *Elec Soc S*, **99**, 86 (2000).

22. M. Guo and R. E. White, *J Power Sources*, **198**, 322 (2012).

23. X. Hu, S. Stanton, L. Cai and R. E. White, *J Power Sources*, **214**, 40 (2012).

24. S. Renganathan and R. E. White, *J Power Sources*, **196**, 442 (2011).

25. M. Wang, X. R. Xiao and X. S. Huang, *J Power Sources*, **307**, 77 (2016).

26. J. Christensen and J. Newman, *J Solid State Electr*, **10**, 293 (2006).

27. U. Kasavajjula, C. S. Wang and A. J. Appleby, *J Power Sources*, **163**, 1003 (2007).

28. D. Larcher, S. Beattie, M. Morcrette, K. Edstroem, J. C. Jumas and J. M. Tarascon, *J Mater Chem*, **17**, 3759 (2007).

29. M. N. Obrovac, L. Christensen, D. B. Le and J. R. Dahnb, *J Electrochem Soc*, **154**, A849 (2007).

30. X. H. Liu, L. Zhong, S. Huang, S. X. Mao, T. Zhu and J. Y. Huang, *Acs Nano*, **6**, 1522 (2012).

31.   K. Zhao, W. L. Wang, J. Gregoire, M. Pharr, Z. Suo, J. J. Vlassak and E. Kaxiras, *Nano letters*, **11**, 2962 (2011).

32.   Y. T. Bie, J. Yang, W. Lu, Z. H. Lei, Y. N. Nuli and J. L. Wang, *Electrochim Acta*, **212**, 141 (2016).

33.   M. H. Braga, A. Debski and W. Gasior, *J Alloy Compd*, **616**, 581 (2014).

34.   V. L. Chevrier, J. W. Zwanziger and J. R. Dahn, *J Alloy Compd*, **496**, 25 (2010).

35.   A. Debski, W. Zakulski, L. Major, A. Goral and W. Gasior, *Thermochim Acta*, **551**, 53 (2013).

36.   T. Gruber, D. Thomas, C. Roder, F. Mertens and J. Kortus, *J Raman Spectrosc*, **44**, 934 (2013).

37.   J. B. Ratchford, B. E. Schuster, B. A. Crawford, C. A. Lundgren, J. L. Allen and J. Wolfenstine, *J Power Sources*, **196**, 7747 (2011).

38.   G. T. Zhou, O. Palchik, I. Nowik, R. Herber, Y. Koltypin and A. Gedanken, *J Solid State Chem*, **177**, 3014 (2004).

39.   K. Kang, H.-S. Lee, D.-W. Han, G.-S. Kim, D. Lee, G. Lee, Y.-M. Kang and M.-H. Jo, *Applied Physics Letters*, **96**, 053110 (2010).

40.   J. Arai, R. Nakahigashi and T. Sugiyama, *J Electrochem Soc*, **163**, A1064 (2016).

41.   J. Zhang, X. F. Liu, J. Wang, J. L. Shi and Z. Q. Shi, *Electrochim Acta*, **187**, 134 (2016).

42.   P. Ramadass, B. Haran, P. M. Gomadam, R. White and B. N. Popov, *J Electrochem Soc*, **151**, A196 (2004).

43.   K. Higa and V. Srinivasan, *J Electrochem Soc*, **162**, A1111 (2015).

44.   K. C. Kam and M. M. Doeff, *J Mater Chem*, **21**, 9991 (2011).

45. V. B. Shenoy, P. Johari and Y. Qi, *J Power Sources*, **195**, 6825 (2010).

46. L. Y. Beaulieu, K. W. Eberman, R. L. Turner, L. J. Krause and J. R. Dahn, *Electrochem Solid St*, **4**, A137 (2001).

47. P. Limthongkul, Y. I. Jang, N. J. Dudney and Y. M. Chiang, *J Power Sources*, **119**, 604 (2003).

48. P. Limthongkul, Y. I. Jang, N. J. Dudney and Y. M. Chiang, *Acta Mater*, **51**, 1103 (2003).

49. A. Kuhn, P. Sreeraj, R. Pöttgen, H.-D. Wiemhöfer, M. Wilkening and P. Heitjans, *Journal of the American Chemical Society*, **133**, 11018 (2011).

50. J. Griego, M. A. Rodriguez and D. E. Wesolowski, Phase Transition Behavior of a Processed Thermal Battery, in, Sandia National Laboratories (SNL-NM), Albuquerque, NM (United States) (2012).

51. S. Dupke, T. Langer, R. Pöttgen, M. Winter, S. Passerini and H. Eckert, *Physical Chemistry Chemical Physics*, **14**, 6496 (2012).

52. C. J. Wen and R. A. Huggins, *J Solid State Chem*, **37**, 271 (1981).

53. V. A. Sethuraman, M. J. Chon, M. Shimshak, V. Srinivasan and P. R. Guduru, *J Power Sources*, **195**, 5062 (2010).

54. M. J. Chon, V. A. Sethuraman, A. McCormick, V. Srinivasan and P. R. Guduru, *Phys Rev Lett*, **107** (2011).

55. M. N. Obrovac and L. Christensen, *Electrochem Solid St*, **7**, A93 (2004).

56. Y. H. Xu, G. P. Yin and P. J. Zuo, *Electrochim Acta*, **54**, 341 (2008).

57. D. S. M. Iaboni and M. N. Obrovac, *J Electrochem Soc*, **163**, A255 (2016).

58. V. L. Chevrier and J. R. Dahn, *J Electrochem Soc*, **156**, A454 (2009).

59.   T. Yoon, C. C. Nguyen, D. M. Seo and B. L. Lucht, *J Electrochem Soc*, **162**, A2325 (2015).

60.   J. G. Xu, Q. L. Zhang and Y. T. Cheng, *J Electrochem Soc*, **163**, A401 (2016).

61.   A. Tranchot, H. Idrissi, P. X. Thivel and L. Roue, *J Power Sources*, **330**, 253 (2016).

62.   B. D. Polat and O. Keles, *Electrochim Acta*, **187**, 293 (2016).

63.   S. D. Beattie, M. J. Loveridge, M. J. Lain, S. Ferrari, B. J. Polzin, R. Bhagat and R. Dashwood, *J Power Sources*, **302**, 426 (2016).

64.   J. Christensen, *J Electrochem Soc*, **157**, A366 (2010).

65.   Y. Yao, M. T. McDowell, I. Ryu, H. Wu, N. Liu, L. Hu, W. D. Nix and Y. Cui, *Nano letters*, **11**, 2949 (2011).

66.   Y. T. Cheng and M. W. Verbrugge, *J Appl Phys*, **104** (2008).

67.   Y. T. Cheng and M. W. Verbrugge, *J Power Sources*, **190**, 453 (2009).

68.   M. W. Verbrugge and Y. T. Cheng, *J Electrochem Soc*, **156**, A927 (2009).

69.   Y. T. Cheng and M. W. Verbrugge, *J Electrochem Soc*, **157**, A508 (2010).

70.   R. Deshpande, Y. T. Cheng and M. W. Verbrugge, *J Power Sources*, **195**, 5081 (2010).

71.   R. Deshpande, Y. T. Cheng, M. W. Verbrugge and A. Timmons, *J Electrochem Soc*, **158**, A718 (2011).

72.   S. K. Soni, B. W. Sheldon, X. C. Xiao, A. F. Bower and M. W. Verbrugge, *J Electrochem Soc*, **159**, A1520 (2012).

73.   D. R. Baker, M. W. Verbrugge and A. F. Bower, *J Solid State Electr*, **20**, 163 (2016).

74.   X. C. Zhang, A. M. Sastry and W. Shyy, *J Electrochem Soc*, **155**, A542 (2008).

75.   M. Jain and J. W. Weidner, *J Electrochem Soc*, **146**, 1370 (1999).

76.   M. Jain, G. Nagasubramanian, R. G. Jungst and J. W. Weidner, *J Electrochem Soc*, **146**, 4023 (1999).

77.   P. M. Gomadam, J. W. Weidner, R. A. Dougal and R. E. White, *J Power Sources*, **110**, 267 (2002).

78.   P. M. Gomadam and J. W. Weidner, *J Electrochem Soc*, **153**, A179 (2006).

79.   P. M. Gomadam, D. R. Merritt, E. R. Scott, C. L. Schmidt, P. M. Skarstad and J. W. Weidner, *J Electrochem Soc*, **154**, A1058 (2007).

80.   P. M. Gomadam, D. R. Merritt, E. R. Scott, C. L. Schmidt, P. M. Skarstad and J. W. Weidner, *J Power Sources*, **174**, 872 (2007).

81.   R. Chandrasekaran, A. Magasinski, G. Yushin and T. F. Fuller, *J Electrochem Soc*, **157**, A1139 (2010).

82.   R. Chandrasekaran and T. F. Fuller, *J Electrochem Soc*, **158**, A859 (2011).

83.   Y. L. Dai, L. Cai and R. E. White, *J Power Sources*, **247**, 365 (2014).

84.   G. G. Botte, V. R. Subramanian and R. E. White, *Electrochim Acta*, **45**, 2595 (2000).

85.   P. Arora, R. E. White and M. Doyle, *J Electrochem Soc*, **145**, 3647 (1998).

86.   P. Arora, M. Doyle and R. E. White, *J Electrochem Soc*, **146**, 3543 (1999).

87.   J. Newman and W. Tiedemann, *AIChE Journal*, **21**, 25 (1975).

88.   T.-S. Dao, C. P. Vyasarayani and J. McPhee, *J Power Sources*, **198**, 329 (2012).

89.   L. Gao, S. Liu and R. A. Dougal, *IEEE transactions on components and packaging technologies*, **25**, 495 (2002).

90. S. Santhanagopalan, Q. Guo, P. Ramadass and R. E. White, *J Power Sources*, **156**, 620 (2006).

91. G. G. Botte, V. R. Subramanian and R. E. White, *Electrochim Acta*, **45**, 2595 (2000).

92. J. Park, W. Lu and A. M. Sastry, *J Electrochem Soc*, **158**, A201 (2011).

93. S. Kalnaus, K. Rhodes and C. Daniel, *J Power Sources*, **196**, 8116 (2011).

94. S. Renganathan, G. Sikha, S. Santhanagopalan and R. E. White, *J Electrochem Soc*, **157**, A155 (2010).

95. T. R. Garrick, Y. Dai, K. Higa, V. Srinivasan and J. W. Weidner, *Ecs Transactions*, **72**, 11 (2016).

96. S. Mohan, Y. Kim, J. B. Siegel, N. A. Samad and A. G. Stefanopoulou, *J Electrochem Soc*, **161**, A2222 (2014).

97. A. G. Stefanopoulou, S. N. Mohan, Y. K. Kim and J. B. Siegel, Bulk Force In A Battery Pack And Its Application To State Of Charge Estimation, in, Google Patents (2016).

98. S. A. Roberts, H. Mendoza, V. E. Brunini, B. L. Trembacki, D. R. Noble and A. M. Grillet, *Journal of Electrochemical Energy Conversion and Storage*, **13**, 031005 (2016).

99. P. Barai, A. Mistry and P. P. Mukherjee, *Extreme Mechanics Letters*, **9**, 359 (2016).

100. B. Rieger, S. Schlueter, S. V. Erhard and A. Jossen, *J Electrochem Soc*, **163**, A1595 (2016).

101. H. Mendoza, S. A. Roberts, V. E. Brunini and A. M. Grillet, *Electrochim Acta*, **190**, 1 (2016).

102. D. Sauerteig, S. Ivanov, H. Reinshagen and A. Bund, *J Power Sources*, **342**, 939 (2017).

103. K. Takahashi, K. Higa, S. Mair, M. Chintapalli, N. Balsara and V. Srinivasan, *J Electrochem Soc*, **163**, A385 (2016).

104. H. Xie, Q. Zhang, H. Song, B. Shi and Y. Kang, *J Power Sources*, **342**, 896 (2017).

105. T. F. Fuller, M. Doyle and J. Newman, *J Electrochem Soc*, **141**, 1 (1994).

106. M. Doyle and J. Newman, *J Power Sources*, **54**, 46 (1995).

107. M. Doyle and J. Newman, *J Appl Electrochem*, **27**, 846 (1997).

108. P. Arora, M. Doyle, A. S. Gozdz, R. E. White and J. Newman, *J Power Sources*, **88**, 219 (2000).

109. M. Doyle, J. Newman, A. S. Gozdz, C. N. Schmutz and J. M. Tarascon, *J Electrochem Soc*, **143**, 1890 (1996).

110. G. Ning, R. E. White and B. N. Popov, *Electrochim Acta*, **51**, 2012 (2006).

111. D. Zhang, B. N. Popov and R. E. White, *J Electrochem Soc*, **147**, 831 (2000).

112. X. C. Zhang, W. Shyy and A. M. Sastry, *J Electrochem Soc*, **154**, A910 (2007).

113. S. Golmon, K. Maute, S. H. Lee and M. L. Dunn, *Applied Physics Letters*, **97** (2010).

114. K. Persson, V. A. Sethuraman, L. J. Hardwick, Y. Hinuma, Y. S. Meng, A. van der Ven, V. Srinivasan, R. Kostecki and G. Ceder, *J Phys Chem Lett*, **1**, 1176 (2010).

115. G. K. Singh, G. Ceder and M. Z. Bazant, *Electrochim Acta*, **53**, 7599 (2008).

116. P. M. Biesheuvel and M. Z. Bazant, *Physical Review* (2010).

117. M. Doyle, T. Fuller and J. Newman, *J. Electrochemical Society*, **140**, 1526 (1993).

118. T. Fuller, M. Doyle and J. Newman, *J. Electrochemical Society* **141**, 1 (1994).

119. V. Ramadesigan, R. N. Methekar, F. Latinwo, R. D. Braatz and V. R. Subramanian, *J. Electrochem. Soc*, **157** (2010).

120. R. C. Alkire, E. A. G. II and C. W. Tobias, *J. Electrochemical Society*, **116**, 1328 (1969).

121. J. S. Dunning, D. N. Bennison and J. Newman, *J. Electrochemical Society*, **120**, 906 (1973).

122. Y.-T. Cheng and M. Verbrugge, *Journal of Power Sources*, **190**, 453 (2009).

123. J. Christensen and J. Newman, *J. of Solid State Electrochemistry*, **10**, 293 (2006).

124. R. Deshpande, Y. Cheng and M. Verbrugge, *J. Power Sources* **195**, 5081 (2010).

125. J. Park, W. Lu and A. M. Sastry, *J. Electrochemical Society*, **158**, A201 (2011).

126. X. Zhang, A. M. Sastry and W. Shyy, *J. Electrochem. Soc*, **155**, A542 (2008).

127. S. Kalnaus, K. Rhodes and C. Daniel, *J. Power Sources* **196**, 8116 (2011).

128. M. N. Obrovac, L. Christensen, D. B. Le and J. R. Dahn, *J. Electrochemical Society* **154**, A849 (2007).

129. S. Renganathan, G. Sikha, S. Santhanagopalan and R. E. White, *J. Electrochemical Society* **157**, A155 (2010).

130. A. V. d. Ven, C. Marianetti, D. Morgan and G. Ceder, *Solid State Ionics* **135**, 21 (2000).

131. H. H. Liu, J. Rutqvist and J. G. Berryman, *International Journal of Rock Mechanics & Mining Sciences*, **46**, 289 (2009).

132. P. M. Gomadam and J. W. Weidner, *J. Electrochem. Soc*, **153**, A175 (2006).

133. R. Corless, G. Gonnet, D. Hare, D. Jeffrey and D. Knuth, *Advances in Computational Mathematics*, **5**, 329 (1996).

134. M. Abramowitz and I. A. Stegun, p. xiv, Dover Publications, New York, (1965).

135. G. E. Blomgren, *J Electrochem Soc*, **164**, A5019 (2017).

136. P. Slowik, N. Pavlenko and N. Lutsey, (2016).

137. Z. A. Needell, J. McNerney, M. T. Chang and J. E. Trancik, *Nature Energy*, **1**, 16112 (2016).

138. F. Momen, K. M. Rahman, Y. Son and P. Savagian, *SAE International Journal of Alternative Powertrains*, **5**, 286 (2016).

139. W. Kempton, *Nature Energy*, **1**, 16131 (2016).

140. J. M. Fenton, *The Electrochemical Society Interface*, **25**, 29 (2016).

141. S. Hawkins, A. Holmes, D. Ames, K. Rahman and R. Malone, *SAE International Journal of Alternative Powertrains*, **3**, 213 (2014).

142. S. Deilami, A. S. Masoum, P. S. Moses and M. A. Masoum, *IEEE Transactions on Smart Grid*, **2**, 456 (2011).

143. K. Morrow, D. Karner and J. Francfort, *US Department of Energy-Vehicle Technologies Program* (2008).

144. K. Parks, P. Denholm and A. J. Markel, (2007).

145. J. Yang, Y. Takeda, Q. Li, N. Imanishi and O. Yamamoto, *J Power Sources*, **90**, 64 (2000).

146. W. Collins, R. Colman, J. Haywood, M. R. Manning and P. Mote, *Sci Am*, **297**, 64 (2007).

147. J. Cannarella and C. B. Arnold, *J Power Sources*, **245**, 745 (2014).

148. A. Van der Ven, C. Marianetti, D. Morgan and G. Ceder, *Solid State Ionics*, **135**, 21 (2000).

149. K. Higa, S. Wu, D. Y. Parkinson, Y. Fu, S. Ferreira, V. Battaglia and V. Srinivasan, *Submitted to J. Electrochem. Soc.* (2017).

150. T. R. Garrick, X. Huang, V. Srinivasan and J. W. Weidner, *In preparation for J. Electrochem. Soc.* (2017).

151. T. R. Garrick, Y. Dai, K. Higa, X. Huang, V. Srinivasan and J. W. Weidner, in *Meeting Abstracts*, p. 18 (2016).

APPENDIX A. STANDARD CONDUCTIVITY OBTAINED FROM LBNL

Conc. [mol/m^3]	Cond. [S/m]
0	0
100	0.17511
200	0.322535
300	0.444847
400	0.544468
500	0.623678
600	0.684619
700	0.729294
800	0.759579
900	0.777219
1000	0.78384
1100	0.780947
1200	0.769931
1300	0.752073
1400	0.728549
1500	0.700431
1600	0.668695
1700	0.634223
1800	0.597807

1900	0.560156
2000	0.521894
2100	0.483572
2200	0.445667
2300	0.408588
2400	0.372678
2500	0.338221
2600	0.305446
2700	0.27453
2800	0.2456
2900	0.218742
3000	0.194003
3100	0.171394
3200	0.150894
3300	0.132458
3400	0.116016
3500	0.101481
3600	0.088752
3700	0.077716
3800	0.068257
3900	0.060256

APPENDIX B. Diffusivity Obtained from LBNL

Conc. [mol/m^3]	Diff. [m^2/s]
0	6.13E-10
100	5.75E-10
200	5.39E-10
300	5.06E-10
400	4.74E-10
500	4.45E-10
600	4.17E-10
700	3.90E-10
800	3.66E-10
900	3.43E-10
1000	3.21E-10
1100	3.00E-10
1200	2.81E-10
1300	2.63E-10
1400	2.46E-10
1500	2.30E-10
1600	2.15E-10
1700	2.01E-10
1800	1.88E-10
1900	1.76E-10
2000	1.64E-10

2100	1.53E-10
2200	1.43E-10
2300	1.33E-10
2400	1.24E-10
2500	1.16E-10
2600	1.08E-10
2700	1.01E-10
2800	9.38E-11
2900	8.73E-11
3000	8.13E-11
3100	7.56E-11
3200	7.03E-11
3300	6.54E-11
3400	6.07E-11
3500	5.64E-11
3600	5.24E-11
3700	4.86E-11
3800	4.51E-11
3900	4.18E-11

APPENDIX C. LAMBERTW FUNCTION INTERPOLATION

x	f(x)				
0.00E+00	0.00E+00	1.71E-01	1.47E-01	3.47E-01	2.66E-01
5.26E-03	5.23E-03	1.76E-01	1.51E-01	3.52E-01	2.69E-01
9.83E-03	9.74E-03	1.81E-01	1.55E-01	3.57E-01	2.72E-01
1.50E-02	1.48E-02	1.86E-01	1.59E-01	3.62E-01	2.75E-01
2.02E-02	1.98E-02	1.91E-01	1.62E-01	3.67E-01	2.78E-01
2.53E-02	2.47E-02	1.96E-01	1.66E-01	3.72E-01	2.81E-01
3.01E-02	2.92E-02	2.01E-01	1.70E-01	3.77E-01	2.84E-01
3.50E-02	3.39E-02	2.06E-01	1.73E-01	3.82E-01	2.87E-01
4.02E-02	3.86E-02	2.11E-01	1.77E-01	3.87E-01	2.90E-01
4.53E-02	4.33E-02	2.16E-01	1.80E-01	3.92E-01	2.93E-01
5.05E-02	4.81E-02	2.21E-01	1.84E-01	3.97E-01	2.95E-01
5.51E-02	5.23E-02	2.26E-01	1.87E-01	4.02E-01	2.98E-01
6.03E-02	5.70E-02	2.31E-01	1.91E-01	4.07E-01	3.01E-01
6.55E-02	6.16E-02	2.36E-01	1.94E-01	4.12E-01	3.04E-01
7.06E-02	6.61E-02	2.41E-01	1.98E-01	4.17E-01	3.07E-01
7.52E-02	7.01E-02	2.46E-01	2.01E-01	4.22E-01	3.10E-01
8.06E-02	7.48E-02	2.51E-01	2.05E-01	4.27E-01	3.12E-01
8.52E-02	7.87E-02	2.56E-01	2.08E-01	4.32E-01	3.15E-01
9.06E-02	8.33E-02	2.62E-01	2.12E-01	4.37E-01	3.18E-01
9.53E-02	8.73E-02	2.66E-01	2.15E-01	4.42E-01	3.21E-01
1.00E-01	9.17E-02	2.71E-01	2.18E-01	4.47E-01	3.24E-01
1.05E-01	9.58E-02	2.76E-01	2.21E-01	4.52E-01	3.26E-01
1.11E-01	1.00E-01	2.81E-01	2.25E-01	4.57E-01	3.29E-01
1.15E-01	1.04E-01	2.86E-01	2.28E-01	4.62E-01	3.32E-01
1.20E-01	1.08E-01	2.91E-01	2.31E-01	4.68E-01	3.35E-01
1.26E-01	1.12E-01	2.96E-01	2.34E-01	4.72E-01	3.37E-01
1.30E-01	1.16E-01	3.01E-01	2.38E-01	4.77E-01	3.40E-01
1.35E-01	1.20E-01	3.07E-01	2.41E-01	4.82E-01	3.43E-01
1.41E-01	1.24E-01	3.11E-01	2.44E-01	4.88E-01	3.45E-01
1.46E-01	1.28E-01	3.17E-01	2.47E-01	4.92E-01	3.48E-01
1.51E-01	1.32E-01	3.22E-01	2.50E-01	4.98E-01	3.51E-01
1.56E-01	1.36E-01	3.27E-01	2.53E-01	5.02E-01	3.53E-01
1.61E-01	1.40E-01	3.32E-01	2.57E-01	5.08E-01	3.56E-01
1.66E-01	1.44E-01	3.37E-01	2.60E-01	5.13E-01	3.58E-01
		3.42E-01	2.63E-01	5.17E-01	3.61E-01

5.23E-01	3.63E-01	7.29E-01	4.60E-01	9.35E-01	5.43E-01
5.28E-01	3.66E-01	7.34E-01	4.62E-01	9.40E-01	5.45E-01
5.33E-01	3.69E-01	7.39E-01	4.64E-01	9.45E-01	5.47E-01
5.38E-01	3.71E-01	7.44E-01	4.66E-01	9.50E-01	5.49E-01
5.43E-01	3.73E-01	7.49E-01	4.69E-01	9.55E-01	5.51E-01
5.48E-01	3.76E-01	7.54E-01	4.71E-01	9.60E-01	5.52E-01
5.53E-01	3.79E-01	7.59E-01	4.73E-01	9.65E-01	5.54E-01
5.58E-01	3.81E-01	7.64E-01	4.75E-01	9.70E-01	5.56E-01
5.63E-01	3.83E-01	7.69E-01	4.77E-01	9.75E-01	5.58E-01
5.68E-01	3.86E-01	7.74E-01	4.79E-01	9.80E-01	5.60E-01
5.73E-01	3.89E-01	7.79E-01	4.81E-01	9.85E-01	5.62E-01
5.78E-01	3.91E-01	7.84E-01	4.83E-01	9.90E-01	5.64E-01
5.83E-01	3.93E-01	7.89E-01	4.86E-01	9.95E-01	5.65E-01
5.88E-01	3.96E-01	7.94E-01	4.88E-01	1.00E+00	5.67E-01
5.93E-01	3.98E-01	7.99E-01	4.90E-01	1.05E+00	5.84E-01
5.98E-01	4.01E-01	8.04E-01	4.92E-01	1.09E+00	5.98E-01
6.03E-01	4.03E-01	8.09E-01	4.94E-01	1.13E+00	6.14E-01
6.08E-01	4.05E-01	8.14E-01	4.96E-01	1.18E+00	6.30E-01
6.13E-01	4.08E-01	8.19E-01	4.98E-01	1.23E+00	6.44E-01
6.18E-01	4.10E-01	8.24E-01	5.00E-01	1.27E+00	6.58E-01
6.23E-01	4.12E-01	8.29E-01	5.02E-01	1.32E+00	6.72E-01
6.28E-01	4.15E-01	8.34E-01	5.04E-01	1.36E+00	6.86E-01
6.33E-01	4.17E-01	8.39E-01	5.06E-01	1.41E+00	6.99E-01
6.38E-01	4.19E-01	8.44E-01	5.08E-01	1.45E+00	7.13E-01
6.43E-01	4.22E-01	8.49E-01	5.10E-01	1.50E+00	7.25E-01
6.48E-01	4.24E-01	8.54E-01	5.12E-01	1.54E+00	7.38E-01
6.53E-01	4.26E-01	8.59E-01	5.14E-01	1.59E+00	7.51E-01
6.58E-01	4.29E-01	8.64E-01	5.16E-01	1.64E+00	7.63E-01
6.64E-01	4.31E-01	8.70E-01	5.18E-01	1.68E+00	7.73E-01
6.68E-01	4.33E-01	8.74E-01	5.20E-01	1.73E+00	7.86E-01
6.74E-01	4.36E-01	8.79E-01	5.22E-01	1.77E+00	7.97E-01
6.78E-01	4.38E-01	8.84E-01	5.24E-01	1.81E+00	8.09E-01
6.83E-01	4.40E-01	8.90E-01	5.26E-01	1.86E+00	8.19E-01
6.88E-01	4.42E-01	8.94E-01	5.28E-01	1.90E+00	8.30E-01
6.93E-01	4.45E-01	9.00E-01	5.30E-01	1.95E+00	8.41E-01
6.98E-01	4.47E-01	9.05E-01	5.32E-01	2.00E+00	8.52E-01
7.04E-01	4.49E-01	9.09E-01	5.33E-01	2.04E+00	8.61E-01
7.09E-01	4.51E-01	9.15E-01	5.35E-01	2.08E+00	8.72E-01
7.14E-01	4.53E-01	9.20E-01	5.37E-01	2.13E+00	8.82E-01
7.19E-01	4.56E-01	9.25E-01	5.39E-01	2.17E+00	8.91E-01
7.23E-01	4.58E-01	9.30E-01	5.41E-01	2.22E+00	9.01E-01

2.27E+00	9.11E-01	4.12E+00	1.22E+00	5.98E+00	1.43E+00
2.31E+00	9.20E-01	4.17E+00	1.22E+00	6.02E+00	1.43E+00
2.35E+00	9.30E-01	4.21E+00	1.23E+00	6.06E+00	1.44E+00
2.40E+00	9.39E-01	4.26E+00	1.24E+00	6.11E+00	1.44E+00
2.45E+00	9.48E-01	4.30E+00	1.24E+00	6.16E+00	1.45E+00
2.49E+00	9.58E-01	4.35E+00	1.25E+00	6.20E+00	1.45E+00
2.54E+00	9.66E-01	4.39E+00	1.25E+00	6.24E+00	1.46E+00
2.58E+00	9.75E-01	4.44E+00	1.26E+00	6.29E+00	1.46E+00
2.63E+00	9.83E-01	4.48E+00	1.26E+00	6.33E+00	1.46E+00
2.67E+00	9.92E-01	4.53E+00	1.27E+00	6.38E+00	1.47E+00
2.72E+00	1.00E+00	4.57E+00	1.28E+00	6.43E+00	1.47E+00
2.76E+00	1.01E+00	4.62E+00	1.28E+00	6.47E+00	1.48E+00
2.81E+00	1.02E+00	4.66E+00	1.29E+00	6.52E+00	1.48E+00
2.86E+00	1.02E+00	4.71E+00	1.29E+00	6.56E+00	1.49E+00
2.90E+00	1.03E+00	4.75E+00	1.30E+00	6.61E+00	1.49E+00
2.94E+00	1.04E+00	4.80E+00	1.30E+00	6.65E+00	1.49E+00
2.99E+00	1.05E+00	4.84E+00	1.31E+00	6.70E+00	1.50E+00
3.03E+00	1.06E+00	4.89E+00	1.31E+00	6.74E+00	1.50E+00
3.08E+00	1.06E+00	4.93E+00	1.32E+00	6.79E+00	1.51E+00
3.12E+00	1.07E+00	4.98E+00	1.32E+00	6.83E+00	1.51E+00
3.17E+00	1.08E+00	5.03E+00	1.33E+00	6.88E+00	1.51E+00
3.21E+00	1.09E+00	5.07E+00	1.33E+00	6.92E+00	1.52E+00
3.26E+00	1.09E+00	5.11E+00	1.34E+00	6.97E+00	1.52E+00
3.31E+00	1.10E+00	5.16E+00	1.34E+00	7.02E+00	1.53E+00
3.35E+00	1.11E+00	5.21E+00	1.35E+00	7.06E+00	1.53E+00
3.40E+00	1.11E+00	5.25E+00	1.35E+00	7.10E+00	1.53E+00
3.44E+00	1.12E+00	5.30E+00	1.36E+00	7.15E+00	1.54E+00
3.49E+00	1.13E+00	5.34E+00	1.36E+00	7.19E+00	1.54E+00
3.53E+00	1.14E+00	5.39E+00	1.37E+00	7.24E+00	1.54E+00
3.58E+00	1.14E+00	5.43E+00	1.37E+00	7.29E+00	1.55E+00
3.62E+00	1.15E+00	5.48E+00	1.38E+00	7.33E+00	1.55E+00
3.67E+00	1.16E+00	5.52E+00	1.38E+00	7.38E+00	1.56E+00
3.71E+00	1.16E+00	5.57E+00	1.39E+00	7.42E+00	1.56E+00
3.76E+00	1.17E+00	5.62E+00	1.39E+00	7.47E+00	1.56E+00
3.80E+00	1.17E+00	5.66E+00	1.40E+00	7.51E+00	1.57E+00
3.85E+00	1.18E+00	5.70E+00	1.40E+00	7.56E+00	1.57E+00
3.89E+00	1.19E+00	5.75E+00	1.41E+00	7.60E+00	1.57E+00
3.94E+00	1.19E+00	5.80E+00	1.41E+00	7.65E+00	1.58E+00
3.99E+00	1.20E+00	5.84E+00	1.42E+00	7.69E+00	1.58E+00
4.03E+00	1.21E+00	5.88E+00	1.42E+00	7.74E+00	1.59E+00
4.07E+00	1.21E+00	5.93E+00	1.43E+00	7.78E+00	1.59E+00

7.83E+00	1.59E+00	9.68E+00	1.73E+00	2.54E+01	2.37E+00
7.87E+00	1.60E+00	9.73E+00	1.73E+00	2.58E+01	2.38E+00
7.92E+00	1.60E+00	9.78E+00	1.73E+00	2.63E+01	2.40E+00
7.96E+00	1.60E+00	9.82E+00	1.73E+00	2.67E+01	2.41E+00
8.01E+00	1.61E+00	9.86E+00	1.74E+00	2.72E+01	2.42E+00
8.06E+00	1.61E+00	9.91E+00	1.74E+00	2.76E+01	2.43E+00
8.10E+00	1.61E+00	9.96E+00	1.74E+00	2.81E+01	2.44E+00
8.15E+00	1.62E+00	1.00E+01	1.75E+00	2.86E+01	2.45E+00
8.19E+00	1.62E+00	1.05E+01	1.78E+00	2.90E+01	2.47E+00
8.24E+00	1.62E+00	1.09E+01	1.80E+00	2.94E+01	2.48E+00
8.28E+00	1.63E+00	1.13E+01	1.83E+00	2.99E+01	2.49E+00
8.33E+00	1.63E+00	1.18E+01	1.85E+00	3.03E+01	2.50E+00
8.37E+00	1.63E+00	1.23E+01	1.88E+00	3.08E+01	2.51E+00
8.42E+00	1.64E+00	1.27E+01	1.90E+00	3.12E+01	2.52E+00
8.46E+00	1.64E+00	1.32E+01	1.92E+00	3.17E+01	2.53E+00
8.51E+00	1.64E+00	1.36E+01	1.95E+00	3.21E+01	2.54E+00
8.55E+00	1.65E+00	1.41E+01	1.97E+00	3.26E+01	2.55E+00
8.60E+00	1.65E+00	1.45E+01	1.99E+00	3.31E+01	2.56E+00
8.64E+00	1.65E+00	1.50E+01	2.01E+00	3.35E+01	2.57E+00
8.69E+00	1.66E+00	1.54E+01	2.03E+00	3.40E+01	2.58E+00
8.73E+00	1.66E+00	1.59E+01	2.05E+00	3.44E+01	2.59E+00
8.78E+00	1.66E+00	1.64E+01	2.07E+00	3.49E+01	2.60E+00
8.83E+00	1.67E+00	1.68E+01	2.08E+00	3.53E+01	2.61E+00
8.87E+00	1.67E+00	1.73E+01	2.10E+00	3.58E+01	2.62E+00
8.91E+00	1.67E+00	1.77E+01	2.12E+00	3.62E+01	2.62E+00
8.96E+00	1.68E+00	1.81E+01	2.14E+00	3.67E+01	2.63E+00
9.01E+00	1.68E+00	1.86E+01	2.15E+00	3.71E+01	2.64E+00
9.05E+00	1.68E+00	1.90E+01	2.17E+00	3.76E+01	2.65E+00
9.10E+00	1.69E+00	1.95E+01	2.19E+00	3.80E+01	2.66E+00
9.14E+00	1.69E+00	2.00E+01	2.20E+00	3.85E+01	2.67E+00
9.18E+00	1.69E+00	2.04E+01	2.22E+00	3.89E+01	2.68E+00
9.23E+00	1.69E+00	2.08E+01	2.23E+00	3.94E+01	2.69E+00
9.28E+00	1.70E+00	2.13E+01	2.25E+00	3.99E+01	2.69E+00
9.32E+00	1.70E+00	2.17E+01	2.26E+00	4.03E+01	2.70E+00
9.37E+00	1.70E+00	2.22E+01	2.28E+00	4.07E+01	2.71E+00
9.41E+00	1.71E+00	2.27E+01	2.29E+00	4.12E+01	2.72E+00
9.46E+00	1.71E+00	2.31E+01	2.31E+00	4.17E+01	2.73E+00
9.50E+00	1.71E+00	2.35E+01	2.32E+00	4.21E+01	2.73E+00
9.55E+00	1.72E+00	2.40E+01	2.33E+00	4.26E+01	2.74E+00
9.59E+00	1.72E+00	2.45E+01	2.35E+00	4.30E+01	2.75E+00
9.64E+00	1.72E+00	2.49E+01	2.36E+00	4.35E+01	2.76E+00

4.39E+01	2.76E+00
4.44E+01	2.77E+00
4.48E+01	2.78E+00
4.53E+01	2.79E+00
4.57E+01	2.79E+00
4.62E+01	2.80E+00
4.66E+01	2.81E+00
4.71E+01	2.82E+00
4.75E+01	2.82E+00
4.80E+01	2.83E+00
4.84E+01	2.84E+00
4.89E+01	2.84E+00
4.93E+01	2.85E+00
4.98E+01	2.86E+00
5.03E+01	2.86E+00